

## Evaluation of High-Resolution Precipitation Products over the Rwenzori Mountains (Uganda)

FALUKU NAKULOPA,<sup>a</sup> INNE VANDERKELEN,<sup>a</sup> JONAS VAN DE WALLE,<sup>b</sup> NICOLE P. M. VAN LIPZIG,<sup>b</sup> HOSSEIN TABARI,<sup>c</sup> LIESBET JACOBS,<sup>b,d</sup> COLLINS TWEHEYO,<sup>e</sup> OLIVIER DEWITTE,<sup>f</sup> AND WIM THIERY<sup>a</sup>

<sup>a</sup> *Department of Hydrology and Hydraulic Engineering, Vrije Universiteit Brussel, Brussels, Belgium*

<sup>b</sup> *Department of Earth and Environmental Sciences, KU Leuven, Leuven, Belgium*

<sup>c</sup> *Department of Civil Engineering, KU Leuven, Leuven, Belgium*

<sup>d</sup> *Institute for Biodiversity and Ecosystem Dynamics, University of Amsterdam, Amsterdam, Netherlands*

<sup>e</sup> *Mountains of the Moon University, Fort Portal, Uganda*

<sup>f</sup> *Department of Earth Sciences, Royal Museum for Central Africa, Tervuren, Belgium*

(Manuscript received 30 May 2021, in final form 29 December 2021)

**ABSTRACT:** The Rwenzori Mountains, in southwest Uganda, are prone to precipitation-related hazards such as flash floods and landslides. These natural hazards highly impact the lives and livelihoods of the people living in the region. However, our understanding of the precipitation patterns and their impact on related hazardous events and/or agricultural productivity is hampered by a dearth of in situ precipitation observations. Here, we propose an evaluation of gridded precipitation products as potential candidates filling this hiatus. We evaluate three state-of-the-art gridded products, the ERA5 reanalysis, IMERG satellite observations, and a simulation from the convection-permitting climate model (CPM), COSMO-CLM, for their ability to represent precipitation totals, timing, and precipitation probability density function. The evaluation is performed against observations from 11 gauge stations that provide at least 2.5 years of hourly and half-hourly data, recorded between 2011 and 2016. Results indicate a poor performance of ERA5 with a persistent wet bias, mostly for stations in the rain shadow of the mountains. IMERG gives the best representation of the precipitation totals as indicated by bias score comparisons. The CPM outperforms both ERA5 and IMERG in representing the probability density function, while both IMERG and the CPM have a good skill in capturing precipitation seasonal and diurnal cycles. The better performance of CPM is attributable to its higher resolution. This study highlights the potential of using IMERG and CPM precipitation estimates for hydrological and impact modeling over the Rwenzori Mountains, preferring IMERG for precipitation totals and CPM for precipitation extremes.

**KEYWORDS:** Precipitation; Remote sensing; Climate models; Reanalysis data; Convective parameterization

### 1. Introduction


East Africa experiences a high variability in precipitation, both in time and space. This variability is amplified by the heterogeneous land cover and complex orography. High variability in precipitation may adversely affect crop yields (Kisembe et al. 2019), energy, and water availability via its impact on river discharge and lake levels (Vanderkelen et al. 2018a), as well as human safety due to intense precipitation events causing flash floods and landslides (Jacobs et al. 2016a,b, 2018; Osuret et al. 2016).

Better understanding and development of sustainable strategies to minimize the related socioeconomic impacts requires the use of accurate precipitation datasets. A dense network of in situ gauge measurements would form the most reliable of such datasets; however, East Africa suffers from rain gauge scarcity. This gauge scarcity is even more prevalent in mountainous areas like the Rwenzori Mountains, in which the complex terrain makes the setup and maintenance of gauging stations difficult.

Consequently, for these regions, precipitation estimates from atmospheric reanalyses, satellites, or climate model simulations are often used as alternative precipitation data sources.

The European Center for Medium-Range Weather Forecasts (ECMWF) is one of the leading developers of atmospheric reanalyses through the ECMWF Re-Analysis (ERA) series (Gibson et al. 1997). Their reanalyses provide estimates of climate variables by assimilating observations into the center's numerical weather prediction model (Hersbach et al. 2020). The resulting datasets have found satisfactory application in climate change studies, climate model evaluations, dynamical downscaling, and extreme weather investigations (Kisembe et al. 2019; Delhasse et al. 2020; Gleixner et al. 2020; Thiery et al. 2017).

ERA5, the fifth generation and latest reanalysis product from ECMWF, is based on the Integrated Forecasting System (IFS) Cy41r2 forecast model (Hersbach et al. 2020). Compared to its predecessor, ERA-Interim, ERA5 includes improved parameterization schemes, larger observational datasets, and a finer resolution, resulting in a better performance (Hersbach et al. 2020, 2019). Over East Africa, ERA5 captures the spatial distribution of precipitation reasonably well, though positive biases are consistently reported, especially over complex terrain (Van de Walle et al. 2020; Gleixner et al. 2020). These biases are mostly inherited from the IFS model, since there are no precipitation observations assimilated over this region.

 Denotes content that is immediately available upon publication as open access.

Corresponding author: Faluku Nakulopa, faluku.nakulopa@ufz.de

DOI: 10.1175/JHM-D-21-0106.1

© 2022 American Meteorological Society. For information regarding reuse of this content and general copyright information, consult the [AMS Copyright Policy](#) ([www.ametsoc.org/PUBSReuseLicenses](http://www.ametsoc.org/PUBSReuseLicenses)).

Over the African continent, the sign of bias in ERA5 precipitation estimates is not uniform. For instance, while ERA5 is reported to overestimate precipitation over East Africa's highlands, it underestimates precipitation in West Africa, especially over the Guinea Highlands when compared to gridded observations of Climate Research Unit (CRU), Global Precipitation Climatology Centre (GPCC), and satellite estimates of Climate Hazards Group Infrared Precipitation with Stations (CHIRPS) (Quagraine et al. 2020). Similarly, the performance of ERA5 appears to vary at a regional level too. For example, ERA5 shows a better performance over Tanzania compared to the neighboring Uganda (Gleixner et al. 2020). Whereas, in general, ERA5 has a reduced wet bias in comparison to its predecessor, ERA-Interim, this is not the case for Uganda, where ERA-Interim outperforms ERA5 (Gleixner et al. 2020). This highlights the need to validate ERA5 precipitation estimates locally against local in situ observations.

Van de Walle et al. (2020) evaluated both the Consortium for Small-Scale Modeling in its Climate Mode (COSMO-CLM) simulations and ERA5 against satellite observations over the Lake Victoria basin and noted an overestimation of precipitation by both products. The magnitude of the bias varied over the lake basin, the lake surface, and the mountainous regions, with the largest biases seen over the mountainous region. Compared to COSMO-CLM, ERA5 exhibited the largest biases. Since this study used satellite products as the benchmark, it lacked a comparison with in situ observations.

Satellite products are one of the most known and recognized sources of precipitation estimates. Satellite precipitation estimates are mostly retrieved based on either or both the passive microwave sensors mounted on the low-Earth-orbiting satellites and the thermal infrared sensors mounted on the geostationary satellites. Passive microwave sensors infer information from absorption and scattering properties of hydrometeors in the air (Cui et al. 2020), while infrared sensors base their estimates on cloud-top temperatures (Joyce et al. 2004). The direct interaction with hydrometeors (such as ice particles or raindrops) makes estimates from microwave sensors more accurate compared to those from infrared sensors (Guilleteau et al. 2017; Huffman et al. 2020a). However, the passive microwave sensors face challenges of background emissions and low observation frequency which result in data gaps (Dinku et al. 2011). These gaps are often filled by estimates from infrared sensors, which are available at high temporal resolution (Joyce et al. 2004).

Generally, both sensors suffer limitations as a result of the retrieval processes employed. Notably, mountainous areas like the Rwenzori Mountains present unique challenges to both sensor types. The warm orographic rains in these areas might be underestimated by the infrared sensors as a result of their low temperature threshold (Kimani et al. 2017). Yet again, the presence of frozen surfaces on the mountains may be wrongly interpreted as precipitation by infrared sensors (Cui et al. 2020). Likewise, Petković and Kummerow (2017) reported passive microwave sensors tend to overestimate deep convection; this, in addition to its low effective resolution, leads to poor capture of the subgrid variability in the mountainous areas (Guilleteau et al. 2017).

To feed off the added value of both sensors, most of the recent satellite precipitation products employ a combination of both passive microwave and thermal infrared sensors, optionally supplemented with an active precipitation radar (Huffman et al. 2020a; Kidd et al. 2020). Despite this asset, these products still exhibit underperformance over complex terrain (Monsieurs et al. 2018; Dinku et al. 2011; Dezfuli et al. 2017; Asong et al. 2017; Sungmin and Kirstetter 2018). For example, over the Rwenzori Mountains, both the research and real-time versions of the Tropical Rainfall Measuring Mission (TRMM) 3B42V7 Multisatellite Precipitation Analysis (TMPA) underestimate precipitation amounts (Monsieurs et al. 2018; Diem et al. 2014). The poor performance is mainly attributed to the coarse resolution and the limited overpass time of the satellites, missing some short-lived convective events (Monsieurs et al. 2018).

The recent high-resolution satellite product, the Integrated Multi-satellitE Retrievals for Global Precipitation Measurement (IMERG; Huffman et al. 2020a,b,c) produced by the National Aeronautics and Space Administration (NASA) Goddard Space Flight Center (GSFC) presents improved skill against other satellite products for many regions worldwide (Prakash et al. 2016; Xu et al. 2017; Dezfuli et al. 2017; Asong et al. 2017; Tan et al. 2019a; Sungmin and Kirstetter 2018; Cui et al. 2020). This improvement is attributed to its high resolution, improved morphing system, and the calibration against gauge observations which minimizes biases. The added value of the gauge bias correction is, however, less evident in regions with a poor gauge station network (Sungmin and Kirstetter 2018; Asong et al. 2017).

Despite the improvement IMERG presents, it is reported to underestimate light rainfall, especially in mountainous regions (Xu et al. 2017; Cui et al. 2020; Sahlu et al. 2016). This is in contrast with what Tan et al. (2016) observed in the United States mid-Atlantic region where IMERG overestimates light rainfall while underestimating heavy rains. Over the Ethiopian mountain ranges, IMERG exhibits an underestimation of precipitation amounts with a bias ratio of over 96% (Sahlu et al. 2016). Over the Lake Victoria basin, IMERG version 6 (IMERG V06) better captures the diurnal precipitation cycle compared to TMPA products, with a smaller phase lag of less than 1 h (Tan et al. 2019a). These results highlight the potential of IMERG over East Africa where precipitation is highly convective and spatiotemporally variable.

In addition to reanalysis and satellites, precipitation estimates are obtained from climate model simulations. Climate model simulations provide precipitation estimates by solving mathematical equations that represent dynamical and physical processes in the climate system. On a global scale, global climate models (GCMs) are typically run at resolutions of at least ~100 km and parameterize subgrid processes like radiative transfer, cloud microphysics, turbulence, and convection. These parameterizations induce uncertainties in the representation of fine-scale physical processes and the resulting precipitation estimates (Kim et al. 2014), particularly over tropical areas (Yang et al. 2015; Mukabana and Pielke 1996; Fraedrich 1972; Coe and Bonan 1997). In an effort to reduce the uncertainties in

GCMs, regional climate models (RCMs) are developed to simulate smaller regions and at higher resolutions.

Many RCM simulations analyzed over East Africa show a similar sign in precipitation bias as their driving GCM but generally reduce the magnitude of the bias (Kisembe et al. 2019; Dosio et al. 2019; Thiery et al. 2015; Prein et al. 2013; Akkermans et al. 2014). This improvement can be attributed to the higher resolution, which allows capturing more spatial detail. However, even at high spatial resolutions of ~5–50 km, RCM simulations still face challenges in representing the spatial distribution and diurnal cycle of precipitation, mainly due to the parameterization of convection (Thiery et al. 2015). This necessitates simulations to be conducted at even higher resolutions and with minimal or no parameterization schemes for convection involved.

Simulations at resolutions below ~4 km, at which convection is no longer parameterized, have shown to substantially improve precipitation estimates (Helsen et al. 2020; Kendon et al. 2019; Coppola et al. 2020; Vanden Broucke and Van Lipzig 2017; Vanden Broucke et al. 2019; Tabari et al. 2016; Prein et al. 2015; Meredith et al. 2015; Prein et al. 2013). Such convection-permitting models (CPMs) stand out in capturing precipitation diurnal cycles, extreme precipitation events, and spatial distribution of precipitation, especially over complex terrain (Ban et al. 2014; Fosser et al. 2015; Helsen et al. 2020; Kendon et al. 2019; Prein et al. 2013; Van de Walle et al. 2020; Finney et al. 2020).

Many researchers rely on the aforementioned reanalysis and satellite and climate model simulation precipitation products, despite their shortcomings in performance over complex terrain (Dille et al. 2019; Depicker et al. 2020; Monsieurs et al. 2019; Depicker et al. 2021; Vanderkelen et al. 2018b). Therefore, there is need and necessity to locally validate these gridded precipitation products against in situ observations.

In this study, we perform, for the first time, a gauge observations-based evaluation of three state-of-the-art gridded precipitation products: the ERA5, IMERG V06, and a CPM simulation with the RCM COSMO-CLM over the Rwenzori Mountains and Lake Kivu. The products are consistently evaluated against in situ observations from 11 gauge stations, 10 of which are located at the Rwenzori Mountains and 1 on Lake Kivu. Each station has data spanning on average 2.5 years, recorded between 2011 and 2016. The products are evaluated for their skill to represent the mean precipitation amounts, seasonal and diurnal cycles, precipitation probability density function (PDF), and extreme precipitation indices, whereby several relevant metrics are computed to score the three products objectively.

## 2. Data and methods

### a. Study area

The Rwenzori Mountains, also known as the Mountains of the Moon, are located along the western branch of the East African Rift, at the border between Uganda and the Democratic Republic of Congo. The Mountains get their name from a local phrase “Ruwenzori,” which means “rain maker”

or “cloud king” (Uganda Wildlife Authority 2020). The area represents a key example of a region where precipitation is central to many aspects of life; unfortunately, precipitation patterns in this particular area remain poorly understood.

The Rwenzori Mountains study area extends through the longitudes of 29.0°–30.8°E and latitudes of 0.2°S–1.0°N (Fig. 1). The mountains have a maximum altitude of 5109 m above sea level and cover an area of about 6000 km<sup>2</sup> (Gummert et al. 2016). On average, the mountain range receives over 1500 mm of precipitation per year (Majaliwa et al. 2015). These amounts strongly vary with elevation (Roller et al. 2012; Van de Walle et al. 2020) and the prevailing wind (Thiery et al. 2015). The mountain peaks are covered by glaciers and have river tributaries discharging into the White Nile.

Next to the Rwenzori Mountains, we evaluate the precipitation products for a gauge station at Lake Kivu (Fig. A1 in appendix A). Lake Kivu is located south of the Rwenzori Mountains at the border between Rwanda and the Democratic Republic of Congo. It is one of the major African Great Lakes, at an altitude of 1463 m above sea level (MSL), covering an approximate area of 2400 km<sup>2</sup> and having an average depth of 240 m (maximum depth of 485 m) (Kranenburg et al. 2020; Thiery et al. 2014b). Although the four major African Great Lakes hardly influence precipitation beyond their shores, they increase precipitation over the lake surface (+87%) on average (Thiery et al. 2015). This enhancement is highest over Lake Kivu (+145%) (Thiery et al. 2015), and these increased precipitation amounts may trigger flooding through lake backflows. This is one major reason of evaluating precipitation products over Lake Kivu, in addition to the lake having unique long-term in situ meteorological observations, which is not common across the African Great Lakes region. The inclusion of Lake Kivu allows comparison in performance of the products over strong orography and large water bodies in the region.

### b. Data

A total of 11 precipitation gauge stations are used in this study (Table 1). Ten of the stations—with 1-h resolution data—are located across the slopes of the Rwenzori Mountains (Fig. 1) and are managed by the AfReSlide project (Monsieurs et al. 2018). The other gauge station is located at Lake Kivu (Fig. A1), collects observations at half-hourly resolution, and is managed by the EAGLES project (Rooney et al. 2018; Thiery et al. 2014a). Although their exact observation periods and data length differ, each station provides at least 2.5 years of data recorded between 2011 and 2016 (Table 1).

ERA5 precipitation estimates—with a ~31-km spatial and 1-h temporal resolution—are downloaded for the period 2011–16 (Table 2). While precipitation observations are not directly assimilated into ERA5 over Africa (Hersbach et al. 2020), the estimates are indirectly constrained via the assimilation of other meteorological variables into the IFS model. The IFS model employs the upgraded Tiedtke (1993) large-scale cloud scheme (Tompkins et al. 2007; Forbes and Ahlgrimm 2014), and the improved Tiedtke (1989) convection

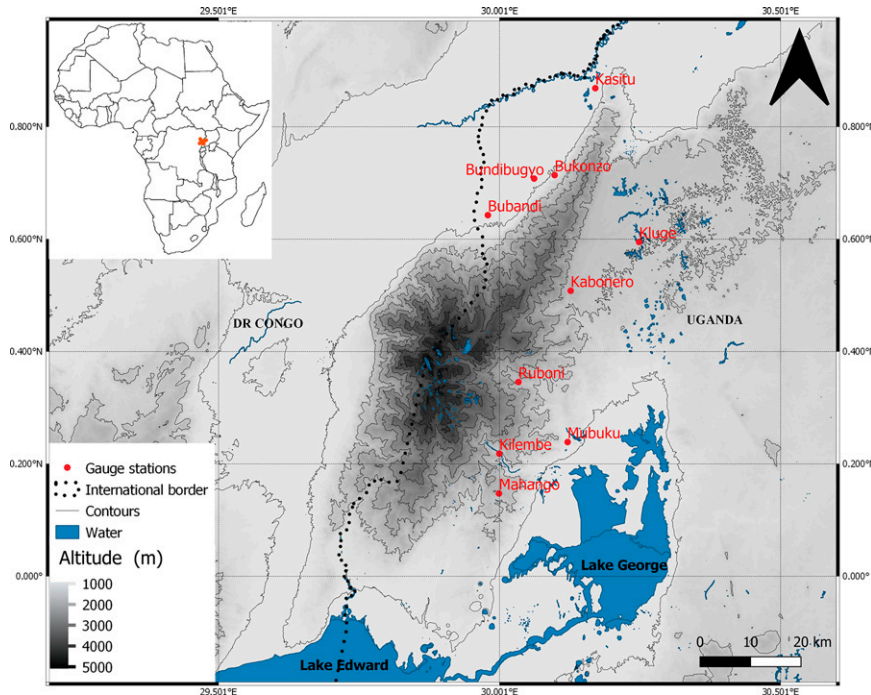


FIG. 1. The Rwenzori Mountains study area. The red points represent the gauge stations. The digital elevation model is obtained from Shuttle Radar Topography Mission Data. The contour lines are at intervals of 500 m. The red cross in the inset at the top left indicates the location of the Rwenzori Mountains on the map of Africa.

parameterization scheme (Hirons et al. 2013a,b) to simulate large-scale and convective precipitation, respectively.

Satellite precipitation estimates are obtained from the GPM. Final run precipitation estimates, precipitationCal, from IMERG V06 are downloaded for the period 2011–16 (Table 2). IMERG is a merged multisatellite gridded precipitation product which replaced the TMPA and provides precipitation estimates from 2000 to present (Huffman 2020; Huffman et al. 2020c). The product uses estimates from multiple satellites such as the TRMM Microwave Imager, GPM Microwave Imager, the Advanced Microwave Scanning Radiometer 2, and the Special

Sensor Microwave Imager/Sounder, etc. (Huffman et al. 2020a). The product has a ~11-km spatial, 30-min temporal resolution and is released in three latencies: an early run, a late run, and the final run with latency periods of 4 h, 14 h, and 3.5 months, respectively. The algorithm merges and interpolates retrievals from passive microwave and infrared sensors, and calibrates them against precipitation gauge observations (for the final run) (Huffman et al. 2020c). The final run estimates, which are used in this study, are bias corrected using monthly gauge data from the Global Precipitation Climatology Center (GPCC) (Huffman et al. 2020a,c). It is, however, important to note that

TABLE 1. Overview of the gauge stations used in the analysis, the available data length, and mean annual precipitation ( $P$ ) amounts. The ID is the rank of the station according to elevation above sea level. Lake Kivu station is purposely put at the bottom of the table.

| ID | Station name | Longitude  | Latitude  | Elevation (MSL) | Start date  | End date    | Resolution (min) | Mean annual $P$ (mm yr <sup>-1</sup> ) | Source                  |
|----|--------------|------------|-----------|-----------------|-------------|-------------|------------------|--|-------------------------|
| 1  | Mahango      | 30°0'0"E   | 0°8'50"N  | 1907            | 16 Aug 2014 | 28 Apr 2019 | 60               | 814.3                                  | Monsieurs et al. (2018) |
| 2  | Ruboni       | 30°2'4"E   | 0°20'44"N | 1660            | 13 Aug 2014 | 28 Apr 2019 | 60               | 1274.9                                 | Monsieurs et al. (2018) |
| 3  | Kabonero     | 30°7'39"E  | 0°30'29"N | 1652            | 11 Aug 2014 | 7 Apr 2019  | 60               | 945.2                                  | Monsieurs et al. (2018) |
| 4  | Kluge        | 30°14'57"E | 0°35'41"N | 1524            | 9 Oct 2014  | 27 Jan 2018 | 60               | 1001.1                                 | Monsieurs et al. (2018) |
| 5  | Kilembe      | 30°0'2"E   | 0°13'5"N  | 1473            | 17 Aug 2014 | 2 Sep 2018  | 60               | 1282.2                                 | Monsieurs et al. (2018) |
| 7  | Bukonzo      | 30°5'56"E  | 0°42'50"N | 1096            | 26 Aug 2014 | 1 May 2019  | 60               | 1016.5                                 | Monsieurs et al. (2018) |
| 8  | Mubuku       | 30°7'19"E  | 0°14'19"N | 1057            | 12 Oct 2014 | 27 Jan 2018 | 60               | 554.1                                  | Monsieurs et al. (2018) |
| 9  | Bundibugyo   | 30°3'45"E  | 0°42'28"N | 949             | 12 Oct 2014 | 19 Jan 2019 | 60               | 1070.3                                 | Monsieurs et al. (2018) |
| 10 | Bubandi      | 29°58'49"E | 0°38'34"N | 936             | 26 Aug 2014 | 1 May 2019  | 60               | 692.9                                  | Monsieurs et al. (2018) |
| 11 | Kasitu       | 30°10'17"E | 0°52'7"N  | 664             | 26 Aug 2014 | 1 May 2019  | 60               | 931.9                                  | Monsieurs et al. (2018) |
| 6  | Lake Kivu    | 29°14'15"E | 1°43'30"S | 1461            | 9 Oct 2012  | 6 Mar 2019  | 30               | 1167.3                                 | Rooney et al. (2018)    |



TABLE 2. Overview of the gridded precipitation products.

| Product type        | ERA5 reanalysis   | IMERG satellite   | COSMO-CLM CPM              |
|---------------------|---|---|----------------------------|
| Spatial resolution  | 31 km   | 11 km   | 2.8 km                     |
| Temporal resolution | 1 h   | 30 min  | 15 min                     |
| Data period         | 2011–16   | 2011–16   | 2011–16                    |
| Data source         | <a href="https://cds.climate.copernicus.eu">https://cds.climate.copernicus.eu</a> | <a href="https://gpm.nasa.gov/data/">https://gpm.nasa.gov/data/</a> | Van de Walle et al. (2020) |

the gauge stations used in this study are not part of the GPCC dataset, and are, therefore, independent of the calibration of IMERG.

RCM-based precipitation estimates are provided by Van de Walle et al. (2020), who applies the COSMO-CLM over the region in a tropical, convection-permitting configuration (Panitz et al. 2014; Brousse et al. 2020). The one-dimensional Freshwater Lake (FLake) model parameterization scheme is online coupled and complements the default TERRA-ML land surface scheme, whereas for the atmosphere a two-moment cloud microphysics scheme is activated. The model is centered at Lake Victoria and its domain covers both the eastern and western branches of the East African Rift. Initial and boundary conditions of the simulations are provided by the ERA5 reanalysis. The simulations provide precipitation data at a  $\sim 2.8$ -km spatial and 15-min temporal resolution, and span a time period of 2010–16 (including one year of spinup). For simplicity, the convection-permitting simulation from COSMO-CLM is hereafter referred to as CPM.

### c. Methodology

For consistency, all gridded products are remapped to the spatial resolution of the CPM product ( $2.8 \text{ km} \times 2.8 \text{ km}$ ) using second-order conservative remapping (Jones 1999). This remapping technique ensures that the integral of the precipitation amounts reported at the original resolution is conserved.

Except for the spatial distribution comparison, we employ a point-to-grid evaluation due to the limited number of stations that cannot permit regridding the gauge observations without creating severe uncertainties (Camberlin et al. 2019; Liu et al. 2019; Tan et al. 2020). Despite the limitations/challenges of point-to-grid analyses and evaluations, especially for extreme precipitation indices, in our case the approach permits evaluation of the products against unaltered primary data. This is important more so in regions with scanty observations where regridding gauge observations seems impossible or would result in severe uncertainties. Similarly, cross-resolution evaluation approach is still widely employed in climate model evaluations, including studies cited by the Intergovernmental Panel on Climate Change (Chen and Sun 2015; Yatagai et al. 2019; Sillmann et al. 2013) and in the evaluation of many gridded precipitation products (Camberlin et al. 2019; Dulière et al. 2011; Zhang et al. 2009; He et al. 2021; Liu et al. 2019; Ayoub et al. 2020; M. L. Tan et al. 2018; Caparoci Nogueira et al. 2018; Wu et al. 2019; Tan et al. 2020; Ensor and Robeson 2008; Silva et al. 2007; Hewitson and Crane 2005).

In the point-to-grid evaluation, to obtain corresponding grid time series, the product estimates for the grid cell containing the station are extracted. Only time periods available in the corresponding gauge station observations are

considered in the evaluation, except for the spatial distribution analysis for which the entire period of 2011–2016 is used.

The IMERG and CPM data and Lake Kivu observations data series, which are originally at subhourly resolution, are transformed to hourly time scales for the hourly analyses by averaging for the IMERG, and summing for CPM and Lake Kivu. Similarly, all the gauge observations and products estimates are accumulated to daily time scale for the respective daily time-scale analyses.

First, the performance of the precipitation products is evaluated for every gauge station using performance metrics for precipitation totals. The mean bias (Bias) is computed as the average difference between the product estimates and the observations. The mean absolute error (MAE) is computed as the average absolute difference between the product estimates and observations. The mean square error (MSE) averages the squared errors between the product estimates and observations, and the root-mean-square error (RMSE) is computed by taking the root of the squared errors. The Nash–Sutcliffe efficiency (NSE) is used to assess the normalized error variance of the precipitation time series of the products and its values range from  $-\infty$  to 1. A negative value of NSE implies that the mean of the observations has a smaller error variance than the precipitation product. A good performing product has a NSE value above 0.5. The Spearman rank correlation evaluates the monotonicity of the relationship between the product estimates and observations. This coefficient varies between  $-1$  and  $+1$ , with a perfect product having a value of  $+1$ . A value 0 implies that there is no correlation between the product estimates and the observations, and negative values indicate negative correlation. The Perkins skill score (PSS) quantifies the similarity between the probability density functions of the observations and products (Perkins et al. 2007). PSS values range from 0 to  $+1$ , with a perfect product having a value of  $+1$ .

Equations for all performance metrics are provided in appendix B.

In addition to the performance metrics for precipitation means, the performance of the products for extreme precipitation is evaluated using six extreme precipitation indices from the Expert Team on Climate Change Detection and Indices (ETCCDI; Zhang et al. 2011): (i) the monthly maximum 1-day precipitation (Rx1day; mm); (ii) the monthly maximum consecutive 5-day precipitation (Rx5day; mm); (iii) the simple daily intensity index (SDII;  $\text{mm day}^{-1}$ ), representing the ratio of the accumulated precipitation amounts on wet days to the total number of wet days; (iv) the heavy precipitation days (R20mm; days), the average number of days in a year with at least 20 mm of precipitation; (v) the consecutive

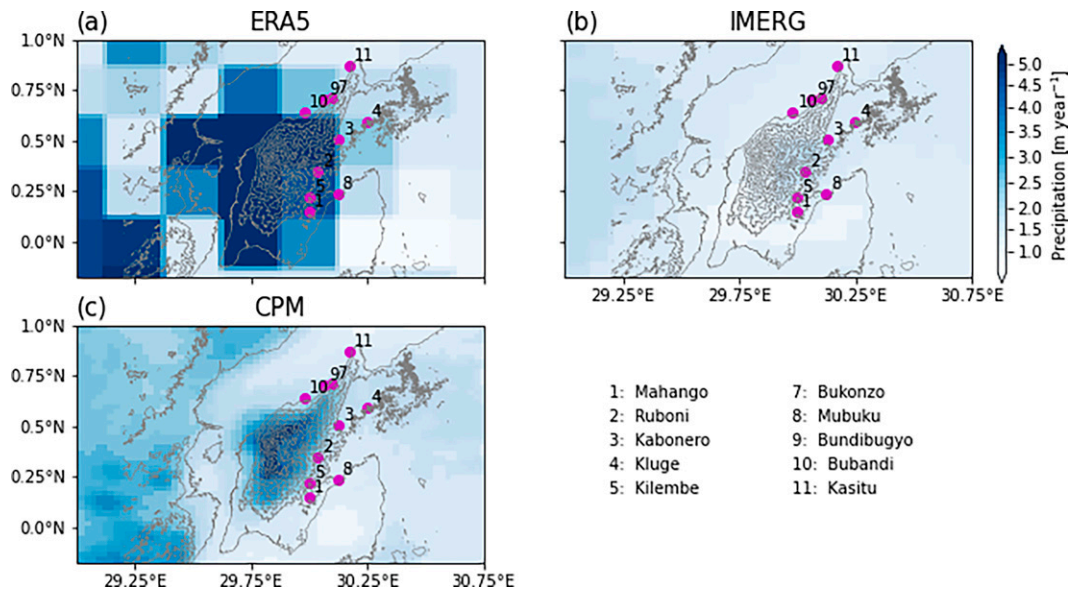


FIG. 2. Mean annual precipitation estimates of (a) ERA5, (b) IMERG, and (c) CPM for the period 2011–16. Gray lines show altitude contours. Purple dots are the gauge stations indicated by their respective number codes, with IDs given in Table 1. For a clearer spatial pattern of IMERG, see Fig. A2, put to a different color scale.

dry days (CDD; days), the average annual maximum number of consecutive days with precipitation less than 1 mm; and (vi) the consecutive wet days (CWD; days), the average annual maximum number of consecutive days with at least 1 mm of precipitation.

Finally, the skill of the products to reproduce observed precipitation intensities is evaluated using PDF plots. We deploy this approach well while cognizant of the uncertainties/challenges associated with point-to-grid cell evaluations, more so in evaluating extremes (Ensor and Robeson 2008; Hewitson and Crane 2005). We, therefore, limit the evaluations to only full-day accumulated precipitation. Accumulation to a larger daily time scale (in our case of 24 time steps for ERA5, 48 for IMERG, and 96 for CPM) minimizes the associated errors and uncertainties (Dulière et al. 2011; Zhang et al. 2009).

### 3. Results

#### a. Evaluation of precipitation totals

All products situate the highest mean annual precipitation totals around the most elevated parts of the Rwenzori Mountains and in the Congo basin. However, the exact location of the precipitation maximums is not unanimous (Fig. 2). ERA5 has its highest precipitation amounts west of the mountain peak, IMERG has it east of the peak, while the CPM precipitation distribution closely follows the altitude profile with higher amounts at higher altitudes. A detailed localization of the precipitation peak is challenging, as the resolution of the products strongly differs. ERA5, for example, has the individual grid cells clearly delineated, yet one can barely see the difference in values for IMERG due to the small range of values (see Fig. A2 for clarity).

Quantitatively, there is a clear difference in the Rwenzori Mountains domain average precipitation totals with ERA5

having the highest domain average of  $3156 \text{ mm yr}^{-1}$ , followed by CPM ( $1930 \text{ mm yr}^{-1}$ ) and last IMERG ( $1268 \text{ mm yr}^{-1}$ ). The large difference among these state-of-the-art products necessitates their evaluation against gauge observations.

Similar to the domain averages, there are large variations in precipitation biases among the products across the different stations (Table 3). ERA5 highly overestimates precipitation at all stations, with biases ranging from  $+104 \text{ mm yr}^{-1}$  at Kasitu to over  $+1900 \text{ mm yr}^{-1}$  at the southeastern stations (Mahango, Ruboni, Kilembe, and Mubuku) and Kabonero station. The mountain stations mean (MTSM) represents an average of the 10 mountain stations, for which ERA5 has a bias of  $+1553 \text{ mm yr}^{-1}$  (+147%). IMERG, in contrast, has both positive and negative biases depending on the station, and consequently the lowest bias of  $-54 \text{ mm yr}^{-1}$  (-5%) for the MTSM. The CPM exhibits generally small biases [with a maximum of  $676 \text{ mm yr}^{-1}$  (+58%) at Bubandi] and has an intermediate bias of  $219 \text{ mm yr}^{-1}$  (+21%) for the MTSM. Consequently, all products, generally, exhibit low correlation with the observations at all stations (Fig. A3).

Besides the mean annual precipitation bias, performance metrics on hourly precipitation for the individual stations also show that ERA5 persistently overestimates precipitation totals since it encompasses the largest values for Bias and MAE at most of the stations (Fig. 3). IMERG has the best skill in estimating the precipitation totals indicated by its better scores in Bias, MAE, MSE, RMSE, NSE, and Spearman rank correlation at all stations. Finally, the CPM outperforms both ERA5 and IMERG in capturing the PDF of the precipitation intensities across all stations as indicated by its high PSS values.

Similar conclusions are drawn when analyzing performance metrics for daily accumulated precipitation (Fig. 4). At daily time scale, the overestimation of precipitation amounts by ERA5 is

TABLE 3. Annual mean precipitation bias and percent relative bias at each station and the mountain stations mean (MTSM).

| Station    | ERA5                        |               | IMERG                       |               | CPM                         |               |
|------------|-----------------------------|---------------|-----------------------------|---------------|-----------------------------|---------------|
|            | Bias (mm yr <sup>-1</sup> ) | Relative bias | Bias (mm yr <sup>-1</sup> ) | Relative bias | Bias (mm yr <sup>-1</sup> ) | Relative bias |
| Mahango    | 2555                        | +314%         | -92                         | -11%          | 208                         | +26%          |
| Ruboni     | 2490                        | +195%         | 13                          | +1%           | 295                         | +23%          |
| Kabonero   | 2018                        | +213%         | 138                         | +15%          | 410                         | +43%          |
| Kluge      | 676                         | +67%          | -38                         | -4%           | 166                         | +17%          |
| Kilembe    | 2473                        | +193%         | -194                        | -15%          | -97                         | -8%           |
| Bukonzo    | 874                         | +86%          | -42                         | -4%           | 436                         | +43%          |
| Mubuku     | 1922                        | +347%         | 204                         | +37%          | 228                         | +41%          |
| Bundibugyo | 568                         | +53%          | -254                        | -24%          | 86                          | +8%           |
| Bubandi    | 1070                        | +154%         | 10                          | +1%           | 400                         | +58%          |
| Kasitu     | 104                         | +11%          | -18                         | -2%           | 123                         | +13%          |
| MTSM       | 1553                        | +147%         | -54                         | -5%           | 219                         | +21%          |
| Kivu       | 1319                        | +113%         | 109                         | +9%           | 676                         | +58%          |

also clearly visible in the large values for Bias, MAE, MSE, and RMSE, especially for the southeastern stations. IMERG still ranks best for most metrics and stations, except for PSS, where CPM holds the best scores. A highly notable feature is that at both hourly and daily time scales, the difference in performance is larger across precipitation products than across stations.

Comparison of the products on a Taylor diagram for the hourly time scale shows that ERA5 and IMERG estimates demonstrate less temporal variability compared to the in situ observations, which leads to an underestimation of the standard deviation at the majority of the stations (Fig. 5a). CPM exhibits the closest agreement with the observations in terms of standard deviation, confirming its ability to capture the PDF of the precipitation intensities as earlier highlighted by the high PSS scores. For most stations, IMERG has the lowest

centered root-mean-square difference (RMSD) values in which both ERA5 and CPM perform poorly. IMERG's better scores in RMSD confirms its good skill in estimating precipitation totals.

The Taylor diagram for the daily time scale estimates (Fig. 5b) shows a similar pattern to that of the hourly estimates, with the exception of the standard deviation which is overestimated by ERA5 for the majority of the stations. From the two diagrams, it is visible that the temporal aggregation from hourly to daily resolution improves the skill of all products in terms of correlation.

b. Seasonal and diurnal cycles

All the products convincingly capture the phase of the observed bimodal seasonal cycle of precipitation with the

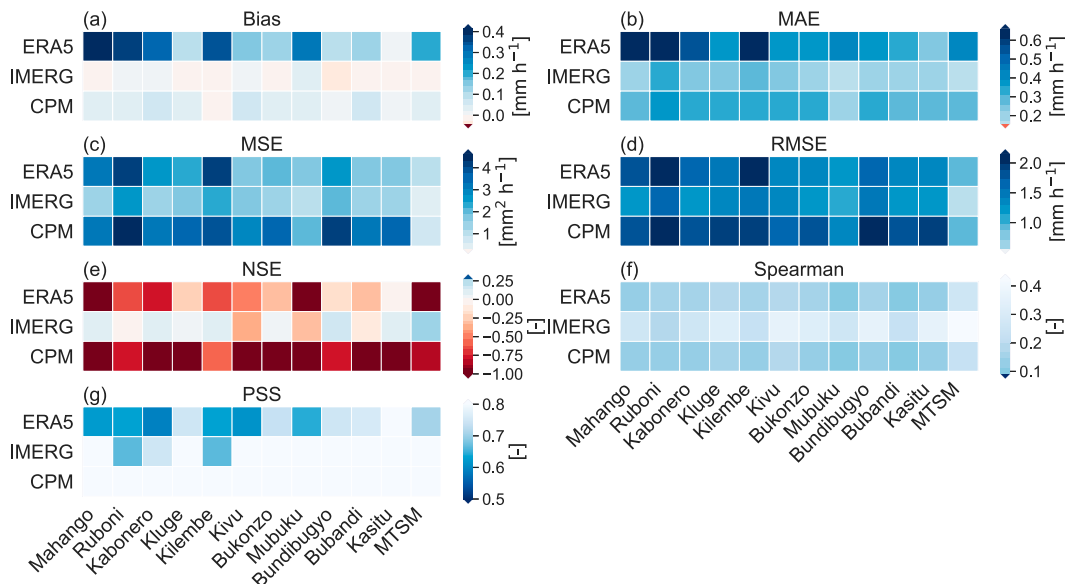


FIG. 3. Performance metrics for hourly precipitation at every station and the mountain stations mean (MTSM). The metrics shown are (a) Bias, (b) mean absolute error (MAE), (c) mean square error (MSE), (d) root-mean-square error (RMSE), (e) Nash–Sutcliffe efficiency (NSE), (f) Spearman rank correlation (Spearman), and (g) Perkins skill score (PSS). Lighter shading indicates better performance.

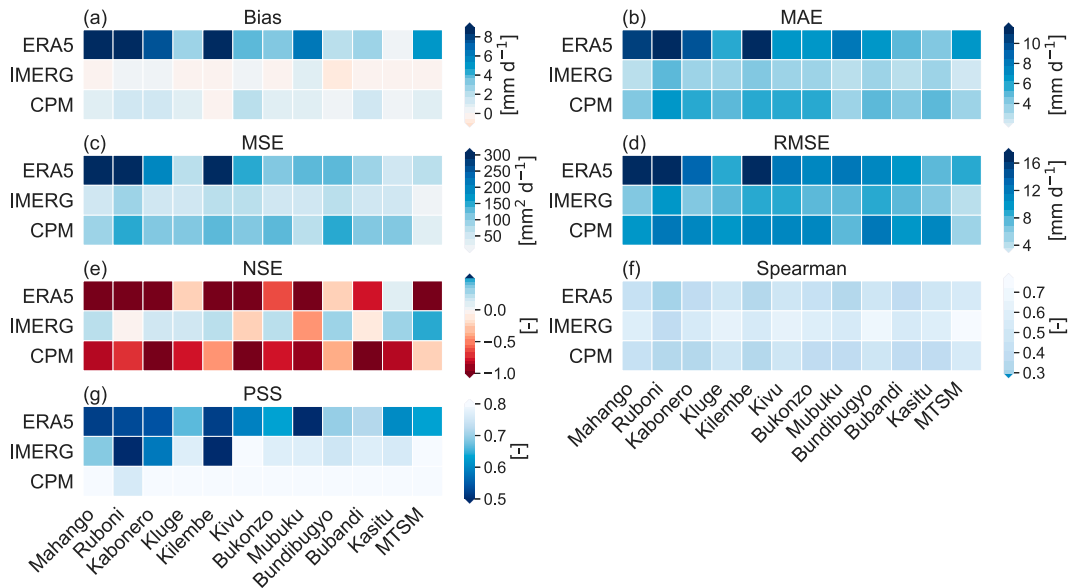


FIG. 4. Performance metrics for daily precipitation for every station and the mountain stations mean (MTSM). The metrics shown are (a) Bias, (b) mean absolute error (MAE), (c) mean square error (MSE), (d) root-mean-square error (RMSE), (e) Nash–Sutcliffe efficiency (NSE), (f) Spearman rank correlation (Spearman), and (g) Perkins skill score (PSS). Lighter shading indicates better performance.

two wet seasons, March–May (long rains) and September–November (short rains), at most stations (Fig. 6). ERA5, however, exhibits a persistent overestimation of the precipitation amplitudes, especially during wet months. This overestimation is strongest at the southern stations and Kabonero station. Different from ERA5, both IMERG and CPM convincingly capture the precipitation amplitudes at the majority of the stations.

Similar to the seasonal cycle, all the products agree on the phase of the diurnal cycle, featuring a prominent afternoon precipitation peak (Fig. 7). ERA5, again, overestimates precipitation amplitudes, especially at the peak hours from 1200 to 2200 local time and at the southeastern stations and Kabonero station. Uniquely, ERA5 exhibits a bimodal peaking within the diurnal cycle with a small depression occurring between 1600 and 2000 local time at all stations. Similarly,

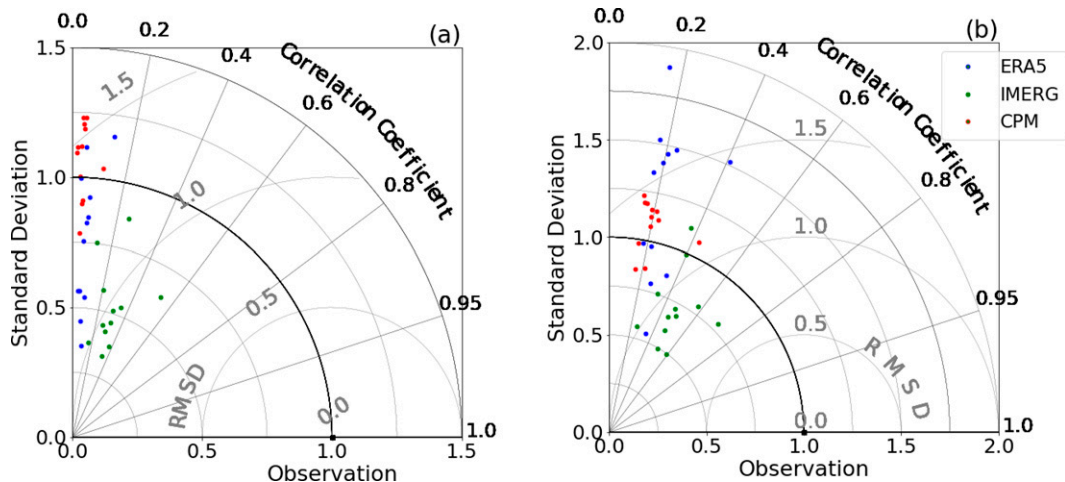


FIG. 5. Taylor diagram showing the performance of the precipitation products: ERA5 (blue dots), IMERG (green dots), and CPM (red dots) for the (a) hourly precipitation and (b) daily precipitation. For every product, each dot represents either a station or the mountain stations mean (MTSM). The gray arcs centered at the origin are for standard deviation, the radial lines indicate the Pearson correlation coefficient, and the gray arcs centered at the 1.0 on the x axis are centered root-mean-square distance (RMSD). The standard deviation and RMSD are normalized by dividing by the standard deviation of the observations.



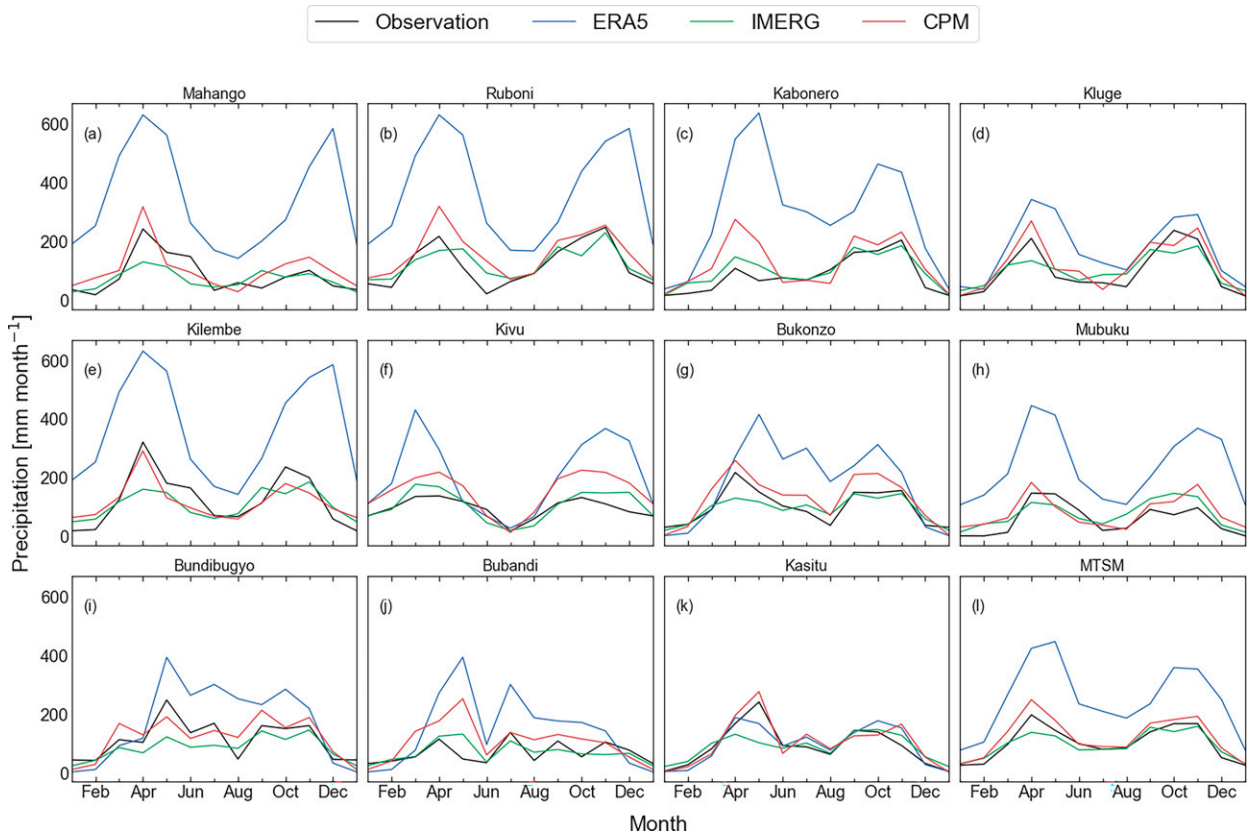


FIG. 6. Precipitation seasonal cycle ( $\text{mm month}^{-1}$ ) for the observations, ERA5, IMERG, and CPM for each station and the mountain stations mean (MTSM). The period over which the data are averaged differs from station (see Table 1).

different from ERA5, both IMERG and CPM show a close agreement in the amplitudes of the diurnal cycle.

### c. Evaluation of extremes

ERA5 exhibits the largest biases in extreme precipitation intensity indices of the Rx1day, Rx5day, and SDII with an overestimation at a majority of the stations mostly for Rx1day and SDII (Fig. 8). There is also visible underestimation at some stations. The sign of the bias depends on the location of the station and the magnitude is highest at the southeastern stations where the biases exceed 15 mm for Rx1day, 50 mm for Rx5day, and  $5 \text{ mm day}^{-1}$  for SDII. These large biases may be because of the relatively coarse resolution of the reanalysis and the small scale of the analyzed events. Additionally, ERA5 also has large positive biases in the number of wet days at all stations and this is also highest at the southeastern stations with positive biases of up to 125 and 50 days for R20mm and CWD, respectively.

Conversely, IMERG generally underestimates extreme precipitation intensity at most stations, as expressed by the negative biases in Rx1day, Rx5day, and SDII. However, it slightly overestimates the number of wet days (R20mm and CWD). CPM has the smallest bias for most indices at the majority stations, which highlights its better skill in capturing extreme precipitation events.

For the CDD, all products unanimously underestimate the length of the dry periods at the southeastern stations as shown by the large negative bias (Fig. 8f). At the rest of the stations, IMERG still underestimates CDD while ERA5 and CPM exhibit a mixed under- and overestimation. For more visualization and comparison, scatterplots for the indices are shown in Fig. A4. Overall, all the products have a higher consistency for the frequency indicators than for the intensity indicators.

CPM outperforms both ERA5 and IMERG in representing the PDF of the precipitation intensities and has the closest agreement observations at all the stations at daily time scale (Fig. 9). ERA5 overestimates the frequency of all intensities at the majority of stations while IMERG shows a close agreement for intensities below  $10 \text{ mm day}^{-1}$  and underestimates for higher intensities. This better performance of CPM in capturing extreme precipitation indicators still manifests when looking into how the products capture the dry days; it is generally the closest to the observations (Table A1 in appendix A).

Across the evaluations, all the products show no noticeable difference in performance at Lake Kivu relative to the mountain stations. This is apparent from the comparable skill with the rest of the stations as visualized in the metrics heat maps, cycle plots, climate extreme indices, and the PDF plots (Figs. 3, 4, 6–10).

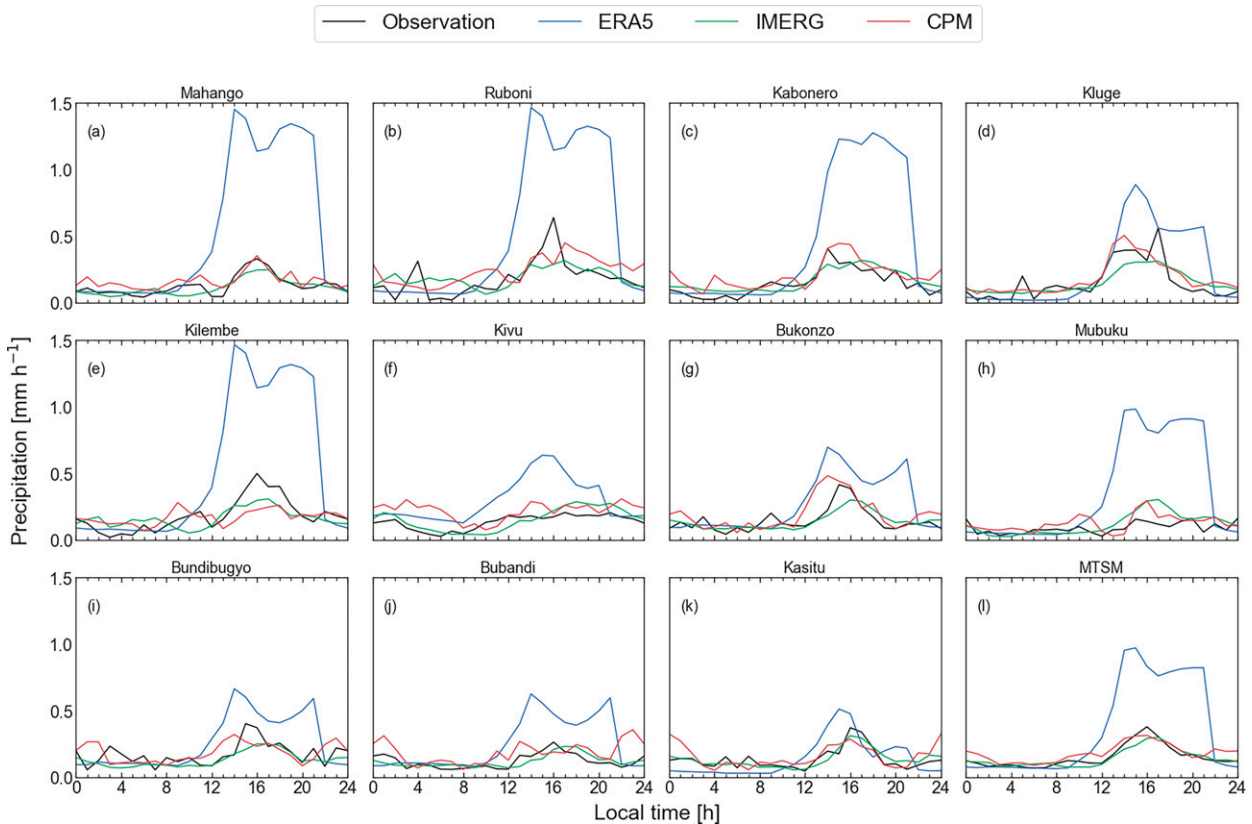


FIG. 7. Diurnal cycles of precipitation for the observations, ERA5, IMERG, and CPM for each gauge station and the mountain stations mean (MTSM). The period over which the data are averaged is station dependent (see Table 1).

#### 4. Discussion

With too high precipitation amounts, large biases in the amplitudes of the diurnal cycle, and underestimation of the frequency of intense precipitation events, ERA5 poorly represents precipitation in the Rwenzori Mountains. Two reasons could explain this performance: (i) the direct effect of evaluating a coarse-resolution gridded product against point observations (Brisson et al. 2016), and (ii) the convection parameterization scheme employed in IFS (Zhang et al. 2016; Hersbach et al. 2020). The coarse resolution implies that some subgrid scale features such as orography-triggered convection and rain-shadow effects are poorly represented (Zhang et al. 2016). The study identifies the hilltops to receive the highest amounts of precipitation and consequently, precipitation amounts at the gauge stations, which are located on the hillslopes, are overestimated by the ERA5, perhaps due to its low resolution. ERA5's largest biases are at stations southeast of the mountain peak, which corresponds to the rain shadow of the Rwenzori Mountains. It is also clear that stations with larger biases fall in the large blue grid cells on the spatial maps (Fig. 2), suggesting that the spatial scale of our analysis does not benefit coarse-resolution products, and highlighting the need for downscaling and use of high-resolution products.

Additionally, the convection parameterization in ERA5's IFS model could be responsible for the large biases, especially in the amplitudes of the diurnal cycle. Deficiencies in the

parameterization scheme were already shown to miss crucial physical processes triggering orographic convection, such as gravity waves or precipitation drifting, causing substantial biases in precipitation (Hersbach et al. 2020). The biases would be minimized if observations over the region were included in the assimilation; unfortunately, this is not the case here due to the scarcity or lack of observations over the region. ERA5 precipitation estimates in this region are thus largely dependent on the IFS model physics.

IMERG has the best skill in reproducing precipitation means. Globally, such good performance could be attributed to its calibration against the GPCP dataset (Tan et al. 2019b; Huffman et al. 2020a). Over the Rwenzori Mountains it performs well, though in this region, GPCP suffers from data scarcity and unequal station distribution (Schneider et al. 2014). This leaves IMERG mainly dependent on satellite retrievals which come with uncertainties too.

Despite the good performance for the precipitation totals, IMERG exhibits a poor capture of the PDF of the precipitation intensities. This can be explained by three factors: (i) similar to ERA5, the direct effect of evaluating coarse-gridded product against point observation plays a role, though less than ERA5 due to IMERG's higher resolution; (ii) uncertainties in its calibration and morphing algorithms which poorly represent light rain evaporation under clouds and may falsely report anvils as precipitating clouds (Cui et al. 2020); and (iii)

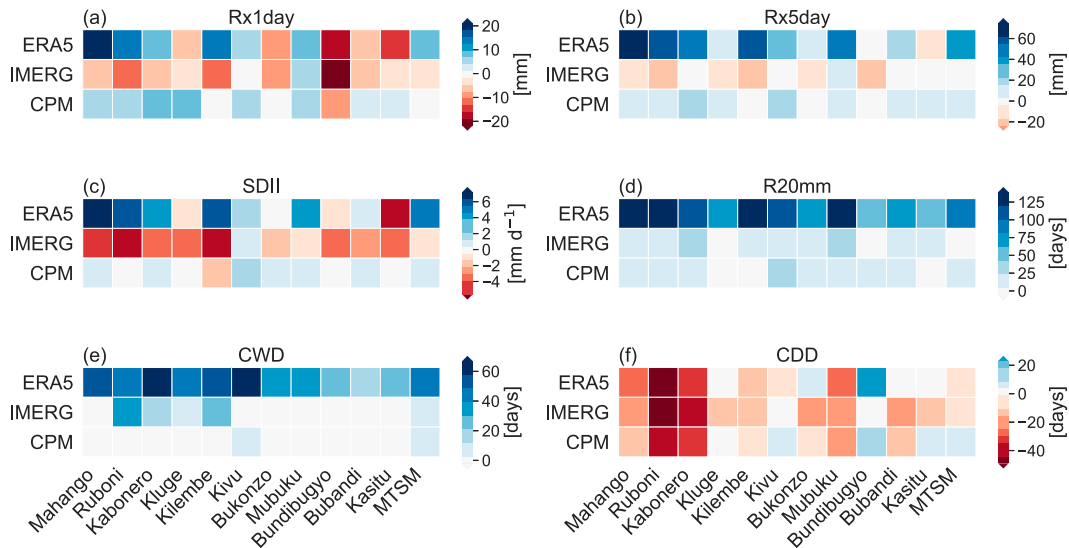


FIG. 8. Bias in extreme precipitation indices (product index minus observation index) for every station and the mountain stations mean (MTSM). The indices shown are (a) monthly maximum 1-day precipitation (Rx1day), (b) monthly maximum 5-day cumulative precipitation (Rx5day), (c) simple daily intensity index (SDII), (d) days with more than 20 mm of precipitation (R20mm), (e) consecutive wet days (CWD), and (f) consecutive dry days (CDD). Lighter shading indicates better performance. See Fig. A4 for the scatterplots.

the overpass gaps of 1–2 h, implying that some short-duration convective events may be missed. The effect of overpass gaps has already been discussed for other satellite products (Monsieurs et al. 2018). The resultant biases would, too, be minimized if the bias correction is done globally and at much higher temporal scales such as the daily adjustments used in the Global Satellite Mapping of Precipitation (GSMaP) dataset (Mega et al. 2014, 2019; X. Tan et al. 2018).

Regarding the generally poor scores of the CPM in the metrics of MSE, NSE, MAE, RMSE, and Spearman correlation, it is important to note that there is no data assimilation in the CPM, and the estimates are based on pure modeling with free running physics in the model domain interior. Therefore, any slight change in the paths and timing of the weather systems may be strongly penalized in these metrics.

CPM outperforms both ERA5 and IMERG in capturing the precipitation PDFs and the extreme precipitation indices. Thanks to its higher resolution, the gridded product versus point observation effect has less impact compared to ERA5 and IMERG. Although it would be expected that ERA5 and IMERG perform better due to the assimilation of observations and calibration against observations, respectively, the higher resolution gives CPM an advantage. This is consistent with results of previous studies, which found a more prominent role of the spatial resolution for extreme precipitation simulations, especially at subdaily time scales (De Troch et al. 2013; Tabari et al. 2016). In our study, as well, a qualitative comparison of PDFs at daily time scale and hourly time scale (Fig. A5 in appendix A) gives CPM a much more advantage at hourly time scale. This indicates that in this region, precipitation fluctuates both in space and

time, and that a product best suited for these conditions has to be of high resolution. For example, design of flood control structures and water infrastructure need precipitation data with spatial and temporal scales of 1–10 km<sup>2</sup> and a few minutes. The coarse-resolution products cannot, thus, be implemented directly in these applications, as they may lead to an underestimation of the design criteria and thereby an increased failure risk (Tabari et al. 2021).

The effect of resolution on the PDF is further investigated by regridding both IMERG and CPM to the ERA5 resolution (~31 km). Lowering the resolution leads to a deterioration of the PDF of both IMERG and CPM (Fig. 10, here shown for the average daily precipitation of the 10 mountain stations). These coarse-resolution regridded IMERG and CPM products overestimate the frequency of light rains and underestimate the frequency of high intensity events. The deterioration effect (qualitatively) is smaller for IMERG compared to CPM due to the smaller difference in resolution in the former.

Notably, even at the coarse resolution of ERA5, CPM (CPM\_E5res) still compares well with higher-resolution IMERG (Fig. 10), probably due to its convection-permitting nature and/or the fact that the effective resolution of the model is finer and therefore some of the benefits of a higher resolution remain even after regridding to coarser resolution. Similarly, the earlier seen good representation of extremes such as the CDD and their timing by CPM could be potentially attributed to the model's convection permitting nature. Avoiding parameterization by explicitly simulating convection has been demonstrated to improve precipitation timing and intensity estimation for many regions worldwide (Prein et al. 2013).

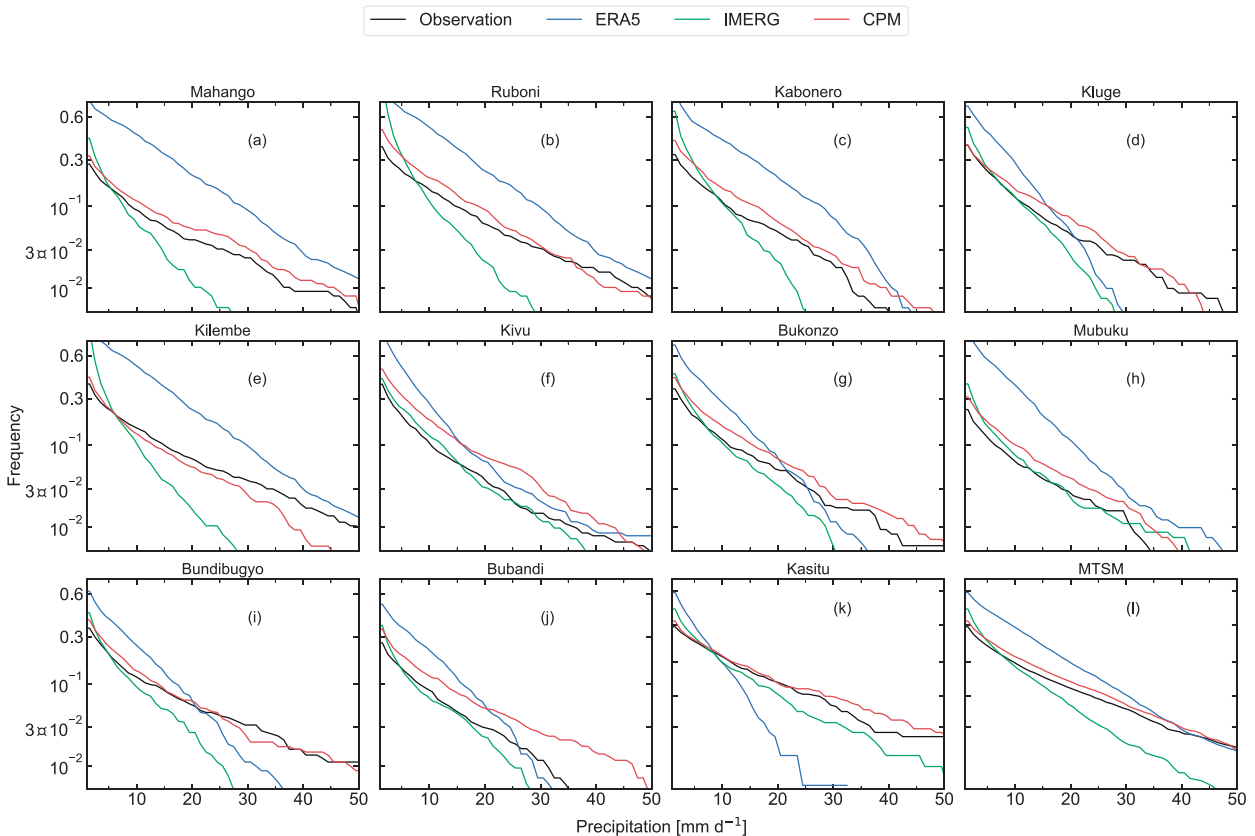


FIG. 9. Probability density function of accumulated daily precipitation, with normalized frequency relative to the total number of days. The x axis is a logarithmic scale.

## 5. Conclusions

Precipitation exhibits high variability both in space and time, and this is especially pronounced for complex terrain of East African areas such as the Rwenzori Mountains. Since these areas are prone to precipitation related hazards and its people mostly thrive on a rain-fed economy, it is important to develop and/or identify accurate precipitation datasets for adequate adaptation planning and disaster risk management. Since in situ observations are scarce, precipitation estimates are mostly inferred from gridded products like reanalysis, satellites, and model simulations. This study evaluates three state-of-the-art precipitation products: ERA5 reanalysis, IMERG satellite estimates, and a convection-permitting simulation (CPM) with COSMO-CLM, against 11 gauge stations observations for a period of at least 2.5 years between 2011 and 2016.

Overall, ERA5 has the poorest performance with a persistent wet bias, most pronounced during the rainy season and for the southeasterly stations located in the rain shadow, and a strong underestimation of the frequency of high extreme events. Possible causes are related to the relatively coarse resolution over complex terrain, and the convection parameterization of its underlying IFS model. IMERG exhibits a good performance in reproducing precipitation totals,

partly attributed to its calibration with gauge data. While CPM outperforms both ERA5 and IMERG in representing the precipitation PDF and extreme precipitation indices, with IMERG and ERA5 overestimating the frequency of light rain and underestimating that of high precipitation. This better performance of CPM is to a greater extent because of its higher resolution compared to ERA5 and IMERG.

For all evaluations and comparisons, there is no outstanding difference between respective product performance at the mountain stations and Lake Kivu station.

Though this study is unique, it being the first to evaluate these three state-of-the-art products against gauge measurements for the Rwenzori Mountains, further research would benefit from longer and recent time series of gauge data. This is particularly important for extreme events assessment, as the accuracy of the IMERG product is shown to increase over time owing to the increasing numbers of passive microwave samples with higher resolutions and more frequency channels. In addition, future studies would benefit from a higher number of gauge stations, preferably well spatially distributed across different elevation levels, as the current gauges are limited to the Ugandan side of the mountains and to elevations below 2000 m above sea level.



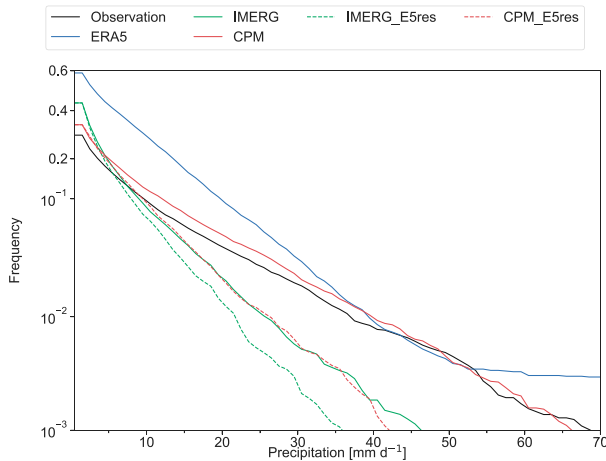


FIG. 10. The average probability density function of the 10 mountain stations including regridDED IMERG (IMERG\_E5res) and CPM (CPM\_E5res) to the resolution of ERA5. The probability density functions are computed on accumulated daily precipitation intensities. The y axis is a logarithmic scale.

Despite these limitations, our study highlights that both IMERG and CPM exhibit a good skill in estimating precipitation totals, as well as seasonal and diurnal cycles. Hence, both products can be used, for example, in the assessment of geohydrological hazard risk such as landslides and flash floods, while preferring CPM for extreme precipitation analysis.

*Acknowledgments.* This work is adapted from Faluku’s master’s degree thesis, which was fully funded by VLIR-UOS. The gauge observations were provided by AfReSlide and the Eagles projects, for which the authors thank Professor Matthieu Kervyn and Dr. Elise Monsieurs. The authors also thank the European Centre for Medium-Range Weather Forecasts (ECMWF) and the National Aeronautics and Space Administration (NASA) for providing the ERA5 reanalysis and IMERG satellite data, respectively. The resources and services used in this work were provided by the Flemish Supercomputer Center (VSC), funded by the Research Foundation—Flanders (FWO) and the Flemish Government. COSMO-CLM integrations were financed by the KU Leuven C1 project “Climate extremes in the Lake Victoria region: The role of urban- and lake-induced dynamics” and were performed on high performance computing facilities of the VSC. The authors are grateful to the CLM community for all their efforts in developing COSMO-CLM and making its code available.

*Data availability statement.* The gauge observations are available upon request. The ERA5 reanalysis data can be accessed from the Copernicus Climate Change Service Climate Data Store (<https://cds.climate.copernicus.eu>), and the IMERG satellite data from the NASA data portal (<https://gpm.nasa.gov/data/>). The convection permitting simulations can be requested from Van de Walle et al. (2020).

TABLE A1. Percentage of dry days, supplementing Fig. 9.

| Station    | Observations (%) | ERA5 (%) | IMERG (%) | CPM (%) |
|------------|------------------|----------|-----------|---------|
| Mahango    | 72.3             | 29.2     | 55.4      | 67.2    |
| Ruboni     | 61.1             | 21.5     | 20.3      | 48.8    |
| Kabonero   | 66.4             | 23.8     | 36.6      | 56.7    |
| Kluge      | 60.1             | 32.4     | 47.9      | 59.8    |
| Kilembe    | 60.2             | 21.4     | 24.3      | 55.4    |
| Bukonzo    | 63.6             | 32.7     | 52.4      | 55.7    |
| Mubuku     | 76.2             | 25.8     | 60.7      | 68.8    |
| Bundibugyo | 64.1             | 37.8     | 53.0      | 58.4    |
| Bubandi    | 73.3             | 47.0     | 61.9      | 64.8    |
| Kasitu     | 71.2             | 41.0     | 56.6      | 66.6    |
| MTSM       | 38.7             | 15.2     | 33.3      | 37.0    |
| Kivu       | 60.4             | 23.4     | 56.7      | 49.5    |

APPENDIX A

Additional Tables and Figures

Table A1 shows the percentage of dry days of each precipitation product for each station and mountain stations mean (MTSM). This table supplements Fig. 9. Dry days are days with less than 1 mm of precipitation. Figure A1 shows the location of the weather station at Lake Kivu, denoted by the red dot on the main map. Lake Kivu is located at the border between the Democratic Republic of Congo (DRC) and Rwanda. It is south of the Rwenzori Mountains as indicated by the black ink below the red cross (the Rwenzori Mountains) in the inset map of Africa (Fig. A1). Figure A2 is the same as Fig. 2b, and it shows the spatial distribution of the mean annual precipitation

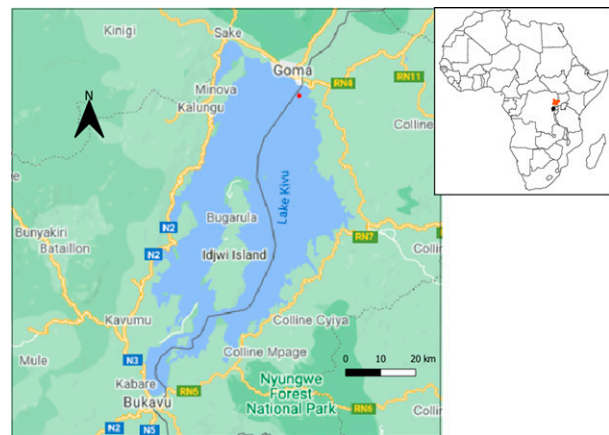


FIG. A1. Location of Lake Kivu. The lower-left corner of the large map is at 28°30’0”N, 2°36’8”W, and the upper-right corner is at 29°36’4”N, 1°30’6”W. The gray line along the lake indicates the border between the Democratic Republic of Congo to the west and Rwanda to the east. The weather station is indicated by the red dot and is situated approximately 3.0 km offshore near Goma. The location of Lake Kivu within Africa is marked on the small (inset) map by a black ink. The red cross in the small map indicates the location of the Rwenzori Mountains.

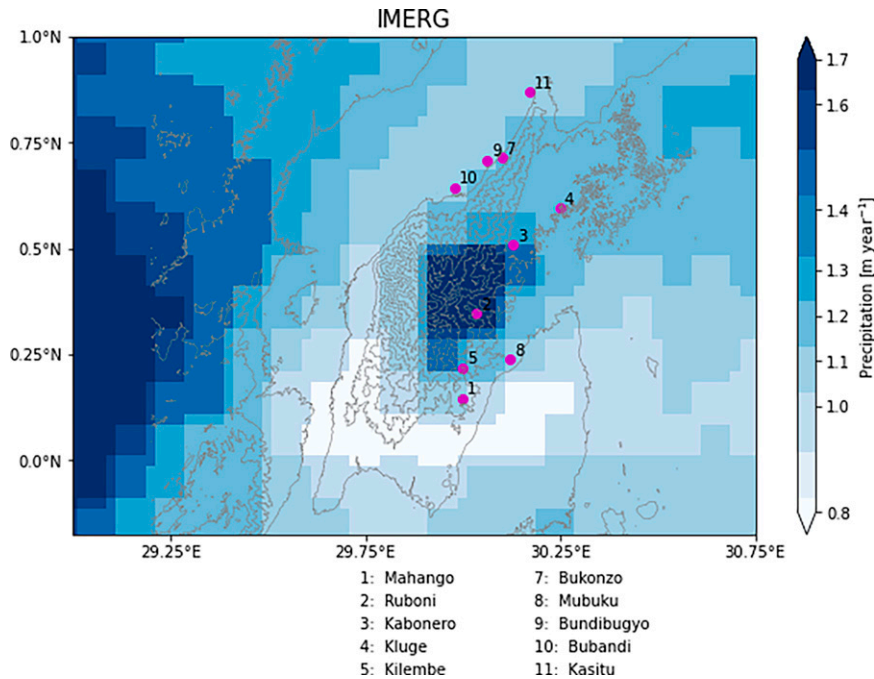


FIG. A2. Mean annual precipitation estimates of IMERG (Fig. 2b) put to its own scale to improve visibility.

estimates of IMERG for the period 2011–16. Different from Fig. 2b, here a different color bar scale is used to better display the spatial distribution of the precipitation which could not be clearly displayed in Fig. 2b due to ERA5's higher value ranges. Figure A3 shows the scatterplots and the respective correlation coefficients between the products (ERA5, IMERG, and CPM) and observations for daily precipitation at all the stations. Similarly, Fig. A4 shows the scatterplots and the respective correlation coefficients between the products' (ERA5, IMERG and CPM) and observations' extreme precipitation indices. This figure enhances the results in Fig. 8. Lastly, Fig. A5 is similar to Fig. 9 but for hourly precipitation values at all the stations and the MTSM.

## APPENDIX B

### Equations of the Performance Metrics

Bias:

$$\text{Bias} = \frac{1}{N} \sum_{n=1}^N (P_n - O_n),$$

where  $N$  is the total number of data pairs of product estimates ( $P$ ) and observations ( $O$ ).

Mean absolute error (MAE):

$$\text{MAE} = \frac{1}{N} \sum_{n=1}^N |P_n - O_n|.$$

Mean square error (MSE):

$$\text{MSE} = \frac{1}{N} \sum_{n=1}^N (P_n - O_n)^2.$$

Root-mean-square error (RMSE):

$$\text{RMSE} = \sqrt{\frac{1}{N} \sum_{n=1}^N (P_n - O_n)^2}.$$

Nash–Sutcliffe efficiency (NSE):

$$\text{NSE} = 1 - \frac{\sum_{n=1}^N (P_n - O_n)^2}{\sum_{n=1}^N (O_n - \bar{O})^2}.$$

Spearman rank correlation (Spearman):

$$\text{Spearman} = \frac{\text{COV}(\text{rP} - \text{rO})}{\sigma_{\text{rP}} \times \sigma_{\text{rO}}}.$$

The Spearman rank correlation is computed as the ratio of the covariance of the difference in the ranks of the product estimates ( $\text{rP}$ ) and observations ( $\text{rO}$ ) to the product of the standard deviations of the ranks ( $\alpha_{\text{rP}}$ ,  $\alpha_{\text{rO}}$ ).

Centered root-mean-square difference (RMSD):

$$\text{RMSD} = \sqrt{\frac{1}{N} \sum_{n=1}^N [(P_n - \bar{P}) - (O_n - \bar{O})]^2},$$

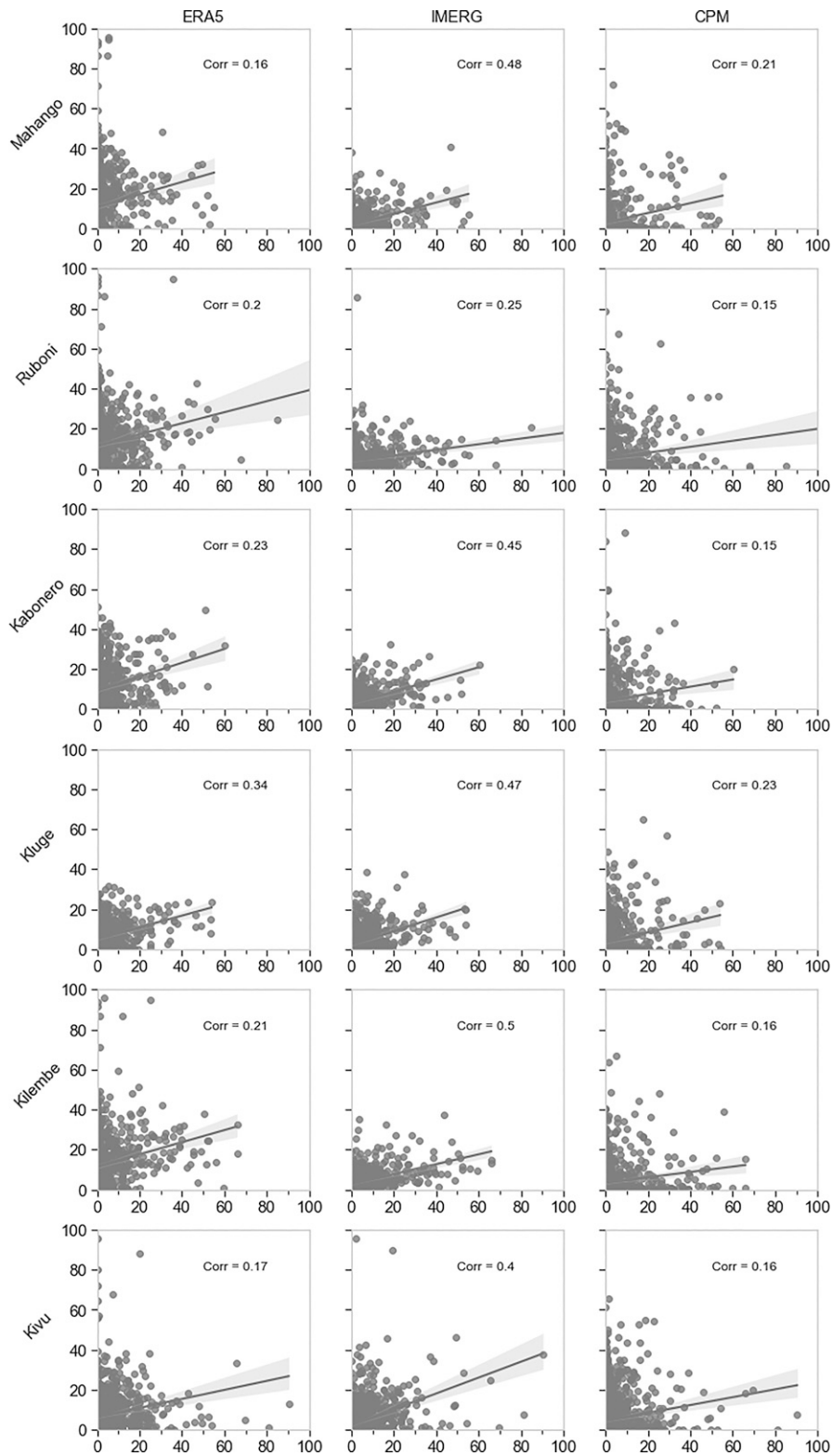


Fig. A3. Scatterplots for the daily precipitation. Each row is for a specific station named on the left of the row. Corr is the Spearman correlation coefficient. For each plot, the product estimate is plotted on the y axis against observations on the x axis. The data are at a daily time step in millimeters.

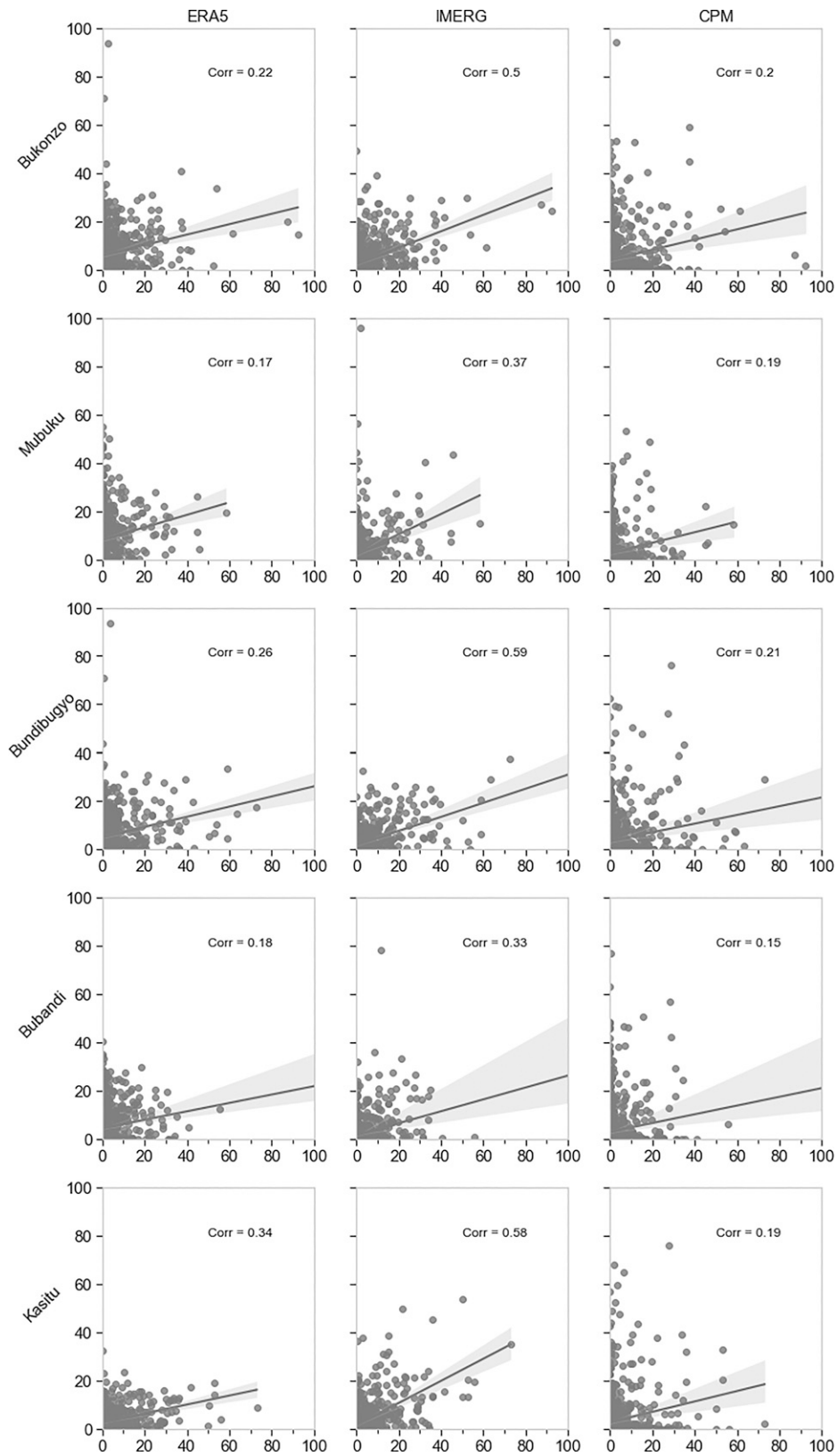


Fig. A3. (Continued)



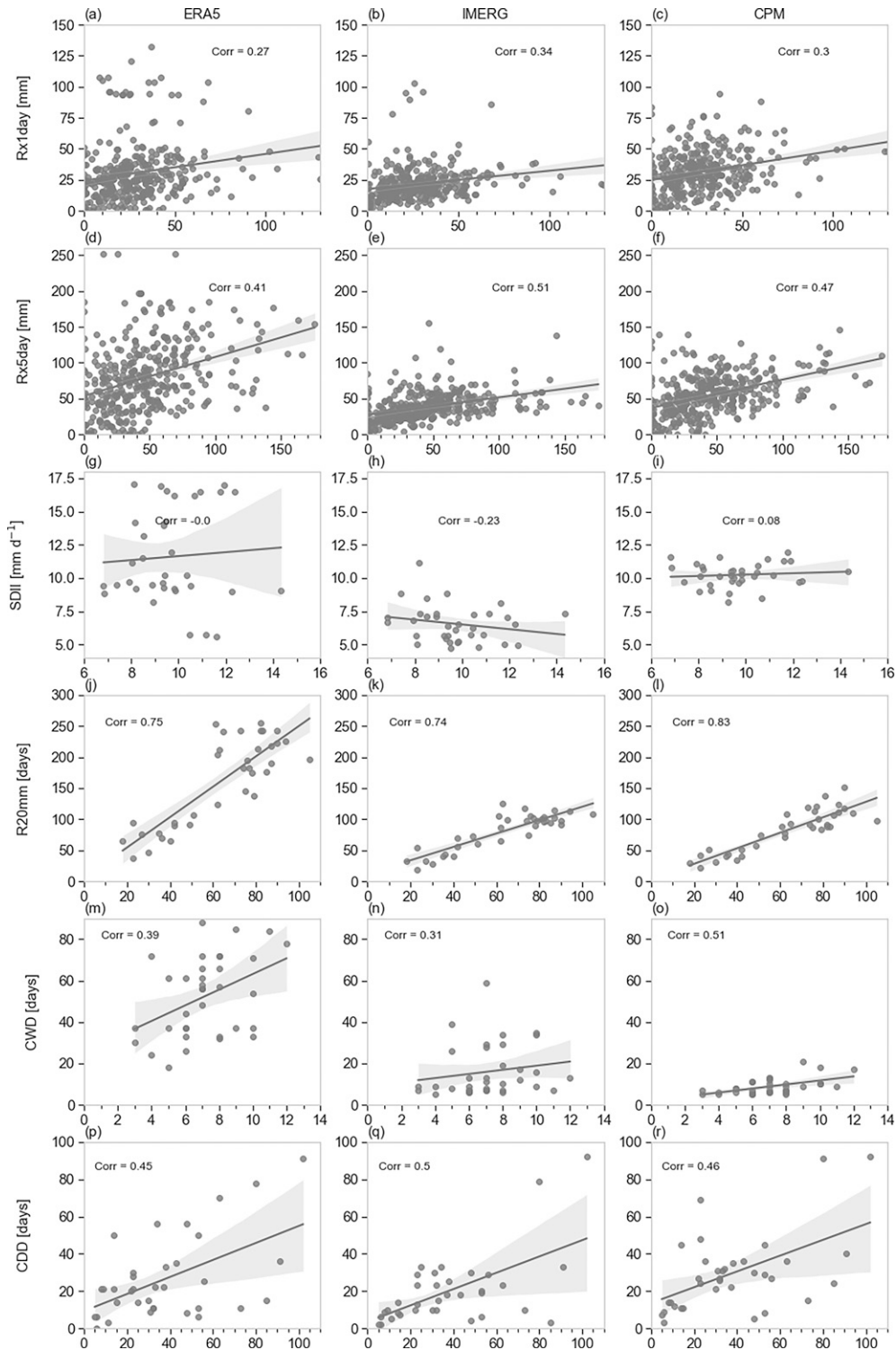


FIG. A4. Scatterplots for the respective extreme precipitation indices. Each row is for a specific index named at the left of the row. Corr is the Spearman correlation coefficient, Rx1day is the monthly maximum 1-day precipitation, Rx5day is the monthly maximum 5-day cumulative precipitation, SDII is the simple daily intensity index, R20mm is the days with more than 20 mm of precipitation, CWD is the consecutive wet days, and CDD is the consecutive dry days. The product's index is plotted on y axis against the observation's index on the x axis. The data are combined for all the 11 stations over the entire time period.

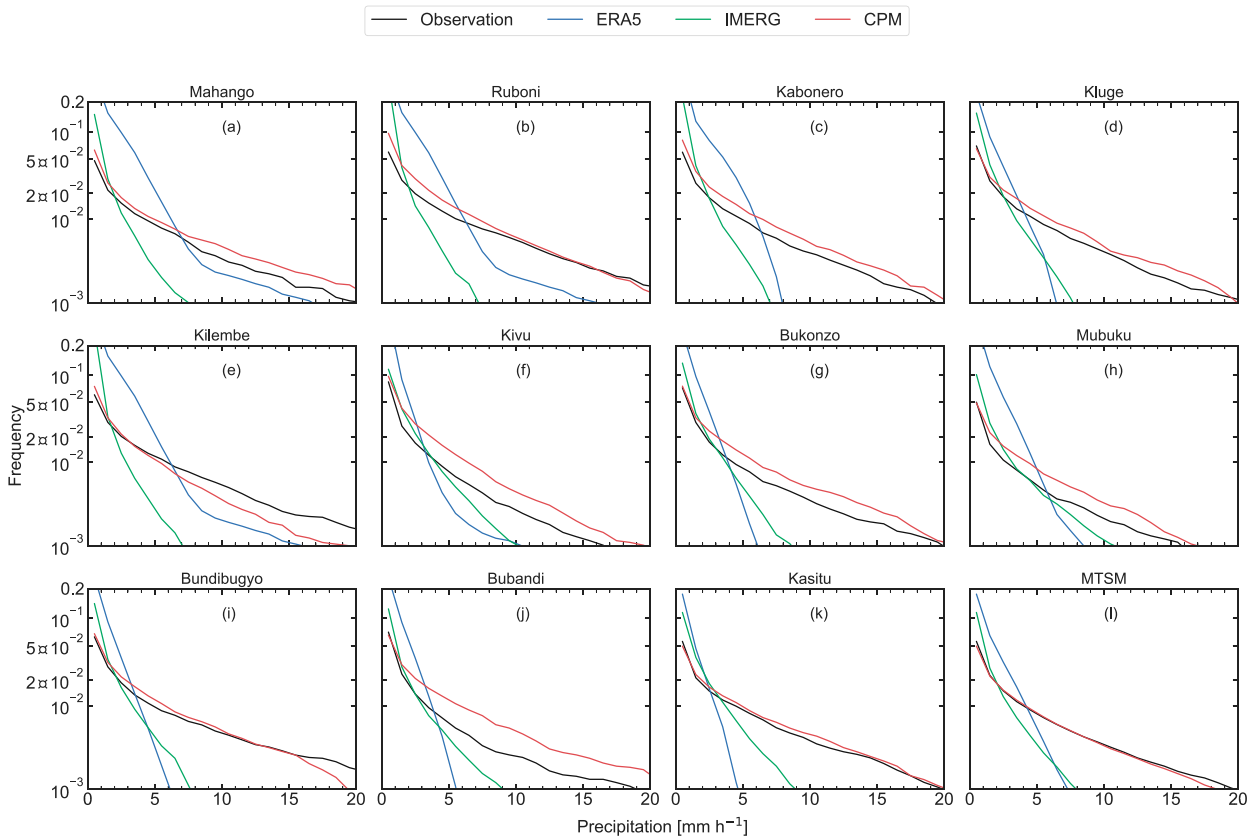


FIG. A5. The probability density function of hourly precipitation, with normalized frequency expressed relative to the total number of hours in the entire study period. The threshold  $0.1 \text{ mm h}^{-1}$  is chosen to select wet from dry conditions/hours. The y axis is a logarithmic scale.

where  $\bar{P}$  and  $\bar{O}$  are the mean precipitation of the product estimates and observations, respectively. It should be noted that RMSD is centered at the mean unlike RMSE.

#### REFERENCES

- Akkermans, T., W. Thiery, and N. P. M. Van Lipzig, 2014: The regional climate impact of a realistic future deforestation scenario in the Congo Basin. *J. Climate*, **27**, 2714–2734, <https://doi.org/10.1175/JCLI-D-13-00361.1>.
- Asong, Z. E., S. Razavi, H. S. Wheeler, and J. S. Wong, 2017: Evaluation of Integrated Multisatellite Retrievals for GPM (IMERG) over southern Canada against ground precipitation observations: A preliminary assessment. *J. Hydrometeorol.*, **18**, 1033–1050, <https://doi.org/10.1175/JHM-D-16-0187.1>.
- Ayoub, A. B., F. Tangang, L. Juneng, M. L. Tan, and J. X. Chung, 2020: Evaluation of gridded precipitation datasets in Malaysia. *Remote Sensing*, **12**, 613, <https://doi.org/10.3390/rs12040613>.
- Ban, N., J. Schmidli, and C. Schär, 2014: Evaluation of the convection-resolving regional climate modeling approach in decade-long simulations. *J. Geophys. Res. Atmos.*, **119**, 7889–7907, <https://doi.org/10.1002/2014JD021478>.
- Brisson, E., K. Van Weverberg, M. Demuzere, A. Devis, S. Saeed, M. Stengel, and N. P. M. Van Lipzig, 2016: How well can a convection-permitting climate model reproduce decadal statistics of precipitation, temperature and cloud characteristics? *Climate Dyn.*, **47**, 3043–3061, <https://doi.org/10.1007/s00382-016-3012-z>.
- Brousse, O., H. Wouters, M. Demuzere, W. Thiery, J. Van de Walle, and N. P. M. Van Lipzig, 2020: The local climate impact of an African city during clear-sky conditions—Implications of the recent urbanization in Kampala (Uganda). *Int. J. Climatol.*, **40**, 4586–4608, <https://doi.org/10.1002/joc.6477>.
- Camberlin, P., and Coauthors, 2019: Evaluation of remotely sensed rainfall products over Central Africa. *Quart. J. Roy. Meteor. Soc.*, **145**, 2115–2138, <https://doi.org/10.1002/qj.3547>.
- Caparoci Nogueira, S. M., M. A. Moreira, and M. M. Lordelo Volpato, 2018: Evaluating precipitation estimates from Eta, TRMM and CHIRPS Data in the south-southeast region of Minas Gerais State - Brazil. *Remote Sensing*, **10**, 313, <https://doi.org/10.3390/rs10020313>.
- Chen, H., and J. Sun, 2015: Assessing model performance of climate extremes in China: An intercomparison between CMIP5 and CMIP3. *Climatic Change*, **129**, 197–211, <https://doi.org/10.1007/s10584-014-1319-5>.
- Coe, M. T., and G. B. Bonan, 1997: Feedbacks between climate and surface water in northern Africa during the middle Holocene. *J. Geophys. Res.*, **102**, 11 087–11 101, <https://doi.org/10.1029/97JD00343>.
- Coppola, E., and Coauthors, 2020: A first-of-its-kind multi-model convection permitting ensemble for investigating convective phenomena over Europe and the Mediterranean. *Climate Dyn.*, **55**, 3–34, <https://doi.org/10.1007/s00382-018-4521-8>.

- Cui, W., X. Dong, B. Xi, Z. Feng, and J. Fan, 2020: Can the GPM IMERG Final product accurately represent MCSs' precipitation characteristics over the central and eastern United States? *J. Hydrometeorol.*, **21**, 39–57, <https://doi.org/10.1175/JHM-D-19-0123.1>.
- Delhasse, A., C. Kittel, C. Amory, S. Hofer, D. Van As, R. S. Fausto, and X. Fettweis, 2020: Brief communication: Evaluation of the near-surface climate in ERA5 over the Greenland Ice Sheet. *Cryosphere*, **14**, 957–965, <https://doi.org/10.5194/tc-14-957-2020>.
- Depicker, A., L. Jacobs, D. Delvaux, H.-B. Havenith, J.-C. Maki Mateso, G. Govers, and O. Dewitte, 2020: The added value of a regional landslide susceptibility assessment: The western branch of the East African Rift. *Geomorphology*, **353**, 106886, <https://doi.org/10.1016/j.geomorph.2019.106886>.
- , G. Govers, L. Jacobs, B. Campforts, J. Uwhirwe, and O. Dewitte, 2021: Interactions between deforestation, landscape rejuvenation, and shallow landslides in the North Tanganyika–Kivu rift region, Africa. *Earth Surf. Dyn.*, **9**, 445–462, <https://doi.org/10.5194/esurf-9-445-2021>.
- De Troch, R., R. Hamdi, H. Van de Vyver, J.-F. Geleyn, and P. Termonia, 2013: Multiscale performance of the ALARO-0 model for simulating extreme summer precipitation climatology in Belgium. *J. Climate*, **26**, 8895–8915, <https://doi.org/10.1175/JCLI-D-12-00844.1>.
- Dezfuli, A. K., C. M. Ichoku, K. I. Mohr, and G. J. Huffman, 2017: Precipitation characteristics in West and East Africa from satellite and in situ observations. *J. Hydrometeorol.*, **18**, 1799–1805, <https://doi.org/10.1175/JHM-D-17-0068.1>.
- Diem, J. E., J. Hartter, S. J. Ryan, and M. W. Palace, 2014: Validation of satellite rainfall products for western Uganda. *J. Hydrometeorol.*, **15**, 2030–2038, <https://doi.org/10.1175/JHM-D-13-0193.1>.
- Dille, A., and Coauthors, 2019: Causes and triggers of deep-seated hillslope instability in the tropics – Insights from a 60-year record of Ikoma landslide (DR Congo). *Geomorphology*, **345**, 106835, <https://doi.org/10.1016/j.geomorph.2019.106835>.
- Dinku, T., P. Ceccato, and S. J. Connor, 2011: Challenges of satellite rainfall estimation over mountainous and arid parts of east Africa. *Int. J. Remote Sensing*, **32**, 5965–5979, <https://doi.org/10.1080/01431161.2010.499381>.
- Dosio, A., R. G. Jones, C. Jack, C. Lennard, G. Nikulin, and B. Hewitson, 2019: What can we know about future precipitation in Africa? Robustness, significance and added value of projections from a large ensemble of regional climate models. *Climate Dyn.*, **53**, 5833–5858, <https://doi.org/10.1007/s00382-019-04900-3>.
- Dulière, V., Y. Zhang, and E. P. Salathé Jr., 2011: Extreme precipitation and temperature over the U.S. Pacific Northwest: A comparison between observations, reanalysis data, and regional models. *J. Climate*, **24**, 1950–1964, <https://doi.org/10.1175/2010JCLI3224.1>.
- Ensor, L. A., and S. M. Robeson, 2008: Statistical characteristics of daily precipitation: Comparisons of gridded and point datasets. *J. Appl. Meteor. Climatol.*, **47**, 2468–2476, <https://doi.org/10.1175/2008JAMC1757.1>.
- Finney, D. L., J. H. Marsham, D. P. Rowell, E. J. Kendon, S. O. Tucker, R. A. Stratton, and L. S. Jackson, 2020: Effects of explicit convection on future projections of mesoscale circulations, rainfall, and rainfall extremes over eastern Africa. *J. Climate*, **33**, 2701–2718, <https://doi.org/10.1175/JCLI-D-19-0328.1>.
- Forbes, R. M., and M. Ahlgrim, 2014: On the representation of high-latitude boundary layer mixed-phase cloud in the ECMWF global model. *Mon. Wea. Rev.*, **142**, 3425–3445, <https://doi.org/10.1175/MWR-D-13-00325.1>.
- Fosser, G., S. Khodayar, and P. Berg, 2015: Benefit of convection permitting climate model simulations in the representation of convective precipitation. *Climate Dyn.*, **44**, 45–60, <https://doi.org/10.1007/s00382-014-2242-1>.
- Fraedrich, K., 1972: A simple climatological model of the dynamics and energetics of the nocturnal circulation at Lake Victoria. *Quart. J. Roy. Meteor. Soc.*, **98**, 322–335, <https://doi.org/10.1002/qj.49709841606>.
- Gibson, J. K., P. Kallberg, A. Hernandez, S. Uppala, A. Nomura, and E. Serrano, 1997: ERA description. ECMWF Re-Analysis Project Rep. Series 1, ECMWF, 72 pp., <https://www.ecmwf.int/node/9584>.
- Gleixner, S., T. Demissie, and G. T. Diro, 2020: Did ERA5 improve temperature and precipitation reanalysis over East Africa? *Atmosphere*, **11**, 996, <https://doi.org/10.3390/atmos11090996>.
- Guiloteau, C., E. Foufoula-Georgiou, and C. D. Kummerow, 2017: Global multiscale evaluation of satellite passive microwave retrieval of precipitation during the TRMM and GPM eras: Effective resolution and regional diagnostics for future algorithm development. *J. Hydrometeorol.*, **18**, 3051–3070, <https://doi.org/10.1175/JHM-D-17-0087.1>.
- Gummert, M., M. Lindenfeld, I. Wölbern, G. Rümpker, K. Celestin, and A. Batte, 2016: Crustal structure and high-resolution Moho topography across the Rwenzori region (Albertine rift) from P-receiver functions. *Geol. Soc. London Spec. Publ.*, **420**, 69–82, <https://doi.org/10.1144/SP420.4>.
- He, Q., J. Yang, H. Chen, J. Liu, Q. Ji, Y. Wang, and F. Tang, 2021: Evaluation of extreme precipitation based on three long-term gridded products over the Qinghai-Tibet Plateau. *Remote Sensing*, **13**, 3010, <https://doi.org/10.3390/rs13153010>.
- Helsen, S., and Coauthors, 2020: Consistent scale-dependency of future increases in hourly extreme precipitation in two convection-permitting climate models. *Climate Dyn.*, **54**, 1267–1280, <https://doi.org/10.1007/s00382-019-05056-w>.
- Hersbach, H., and Coauthors, 2019: Global reanalysis: Goodbye ERA-Interim, hello ERA5. *ECMWF Newsletter*, No. 159, ECMWF, Reading, United Kingdom, 17–24, <https://www.ecmwf.int/node/19027>.
- , and Coauthors, 2020: The ERA5 global reanalysis. *Quart. J. Roy. Meteor. Soc.*, **146**, 1999–2049, <https://doi.org/10.1002/qj.3803>.
- Hewitson, B. C., and R. G. Crane, 2005: Gridded area-averaged daily precipitation via conditional interpolation. *J. Climate*, **18**, 41–57, <https://doi.org/10.1175/JCLI3246.1>.
- Hirons, L., P. Inness, F. Vitart, and P. Bechtold, 2013a: Understanding advances in the simulation of intraseasonal variability in the ECMWF model. Part I: The representation of the MJO. *Quart. J. Roy. Meteor. Soc.*, **139**, 1417–1426, <https://doi.org/10.1002/qj.2060>.
- , —, —, and —, 2013b: Understanding advances in the simulation of intraseasonal variability in the ECMWF model. Part II: The application of process-based diagnostics. *Quart. J. Roy. Meteor. Soc.*, **139**, 1427–1444, <https://doi.org/10.1002/qj.2059>.
- Huffman, G. J., 2020: The transition in multi-satellite products from TRMM to GPM (TMPA to IMERG). Tech. Rep., 5 pp., NASA, <https://gpm.nasa.gov/resources/documents/transition-multi-satellite-products-trmm-gpm-tmpa-imerg>.
- , D. T. Bolvin, D. Braithwaite, K. Hsu, R. Joyce, P. Xie, and S.-H. Yoo, 2020a: NASA Global Precipitation Measurement (GPM) Integrated Multi-satellite Retrievals for GPM

- (IMERG). Algorithm Theoretical Basis Doc., version 06, 35 pp., [https://gpm.nasa.gov/sites/default/files/2020-05/IMERG\\_ATBD\\_V06.3.pdf](https://gpm.nasa.gov/sites/default/files/2020-05/IMERG_ATBD_V06.3.pdf).
- , —, E. J. Nelkin, and J. Tan, 2020b: Integrated Multi-satellite Retrievals for GPM (IMERG) technical documentation. IMERG Tech. Doc., 83 pp., <https://gpm.nasa.gov/resources/documents/IMERG-V06-Technical-Documentation>.
- , and Coauthors, 2020c: Integrated Multi-satellite Retrievals for the Global Precipitation Measurement (GPM) Mission (IMERG). *Satellite Precipitation Measurement*, V. Levizzani et al., Eds., Advances in Global Change Research, Vol. 67, Springer, 343–353, [https://doi.org/10.1007/978-3-030-24568-9\\_19](https://doi.org/10.1007/978-3-030-24568-9_19).
- Jacobs, L., O. Dewitte, J. Poesen, D. Delvaux, W. Thiery, and M. Kervyn, 2016a: The Rwenzori Mountains, a landslide-prone region? *Landslides*, **13**, 519–536, <https://doi.org/10.1007/s10346-015-0582-5>.
- , and Coauthors, 2016b: Reconstruction of a flash flood event through a multi-hazard approach: Focus on the Rwenzori Mountains, Uganda. *Nat. Hazards*, **84**, 851–876, <https://doi.org/10.1007/s11069-016-2458-y>.
- , O. Dewitte, J. Poesen, J. Sekajugo, A. Nobile, M. Rossi, W. Thiery, and M. Kervyn, 2018: Field-based landslide susceptibility assessment in a data-scarce environment: The populated areas of the Rwenzori Mountains. *Nat. Hazards Earth Syst. Sci.*, **18**, 105–124, <https://doi.org/10.5194/nhess-18-105-2018>.
- Jones, P. W., 1999: First-and second-order conservative remapping schemes for grids in spherical coordinates. *Mon. Wea. Rev.*, **127**, 2204–2210, [https://doi.org/10.1175/1520-0493\(1999\)127<2204:FASOCR>2.0.CO;2](https://doi.org/10.1175/1520-0493(1999)127<2204:FASOCR>2.0.CO;2).
- Joyce, R. J., J. E. Janowiak, P. A. Arkin, and P. Xie, 2004: CMORPH: A method that produces global precipitation estimates from passive microwave and infrared data at high spatial and temporal resolution. *J. Hydrometeorol.*, **5**, 487–503, [https://doi.org/10.1175/1525-7541\(2004\)005<0487:CAMTPG>2.0.CO;2](https://doi.org/10.1175/1525-7541(2004)005<0487:CAMTPG>2.0.CO;2).
- Kendon, E. J., R. A. Stratton, S. Tucker, J. H. Marsham, S. Berthou, D. P. Rowell, and C. A. Senior, 2019: Enhanced future changes in wet and dry extremes over Africa at convection-permitting scale. *Nat. Commun.*, **10**, 1794, <https://doi.org/10.1038/s41467-019-09776-9>.
- Kidd, C., Y. N. Takayabu, G. M. Skofronick-Jackson, G. J. Huffman, S. A. Braun, T. Kubota, and F. J. Turk, 2020: The Global Precipitation Measurement (GPM) Mission. *Satellite Precipitation Measurement*, V. Levizzani et al., Eds., Advances in Global Change Research, Vol. 67, Springer, 3–23, [https://doi.org/10.1007/978-3-030-24568-9\\_1](https://doi.org/10.1007/978-3-030-24568-9_1).
- Kim, J., and Coauthors, 2014: Evaluation of the CORDEX-Africa multi-RCM hindcast: Systematic model errors. *Climate Dyn.*, **42**, 1189–1202, <https://doi.org/10.1007/s00382-013-1751-7>.
- Kimani, M. W., J. C. Hoedjes, and Z. Su, 2017: An assessment of satellite-derived rainfall products relative to ground observations over East Africa. *Remote Sensing*, **9**, 430, <https://doi.org/10.3390/rs9050430>.
- Kisembe, J., A. Favre, A. Dosio, C. Lennard, G. Sabiiti, and A. Nimusiima, 2019: Evaluation of rainfall simulations over Uganda in CORDEX regional climate models. *Theor. Appl. Climatol.*, **137**, 1117–1134, <https://doi.org/10.1007/s00704-018-2643-x>.
- Kranenburg, W., and Coauthors, 2020: 3D-modelling of Lake Kivu: Horizontal and vertical flow and temperature structure under spatially variable atmospheric forcing. *J. Great Lakes Res.*, **46**, 947–960, <https://doi.org/10.1016/j.jglr.2020.05.012>.
- Liu, J., D. Shangquan, S. Liu, Y. Ding, S. Wang, and X. Wang, 2019: Evaluation and comparison of CHIRPS and MSWEP daily-precipitation products in the Qinghai-Tibet Plateau during the period of 1981–2015. *Atmos. Res.*, **230**, 104634, <https://doi.org/10.1016/j.atmosres.2019.104634>.
- Majaliwa, J. G. M., and Coauthors, 2015: Characterization of historical seasonal and annual rainfall and temperature trends in selected climatological homogenous rainfall zones of Uganda. *Global J. Sci. Res.*, **15**, 21–40.
- Mega, T., T. Ushio, T. Kubota, M. Kachi, K. Aonashi, and S. Shige, 2014: Gauge adjusted global satellite mapping of precipitation (GSMaP\_Gauge). *2014 XXXIth URSI General Assembly and Scientific Symp. (URSI GASS)*, Beijing, China, Institute of Electrical and Electronics Engineers, 1–4, <https://doi.org/10.1109/URSIGASS.2014.6929683>.
- , —, M. Takahiro, T. Kubota, M. Kachi, and R. Oki, 2019: Gauge-adjusted global satellite mapping of precipitation. *IEEE Trans. Geosci. Remote Sensing*, **57**, 1928–1935, <https://doi.org/10.1109/TGRS.2018.2870199>.
- Meredith, E. P., D. Maraun, V. A. Semenov, and W. Park, 2015: Evidence for added value of convection-permitting models for studying changes in extreme precipitation. *J. Geophys. Res. Atmos.*, **120**, 12 500–12 513, <https://doi.org/10.1002/2015JD024238>.
- Monsieurs, E., and Coauthors, 2018: Evaluating TMPA rainfall over the sparsely gauged East African Rift. *J. Hydrometeorol.*, **19**, 1507–1528, <https://doi.org/10.1175/JHM-D-18-0103.1>.
- , O. Dewitte, and A. Demoulin, 2019: A susceptibility-based rainfall threshold approach for landslide occurrence. *Nat. Hazards Earth Syst. Sci.*, **19**, 775–789, <https://doi.org/10.5194/nhess-19-775-2019>.
- Mukabana, J. R., and R. A. Pielke, 1996: Investigating the influence of synoptic-scale monsoonal winds and mesoscale circulations on diurnal weather patterns over Kenya using a mesoscale numerical model. *Mon. Wea. Rev.*, **124**, 224–244, [https://doi.org/10.1175/1520-0493\(1996\)124<0224:ITIOSS>2.0.CO;2](https://doi.org/10.1175/1520-0493(1996)124<0224:ITIOSS>2.0.CO;2).
- Osuret, J., L. M. Atuyambe, R. W. Mayega, J. Ssentongo, N. Tumuhameye, G. M. Bua, D. Tuhebwe, and W. Bazeyo, 2016: Coping strategies for landslide and flood disasters: A qualitative study of Mt. Elgon Region, Uganda. *PLOS Curr.*, **8**, <https://doi.org/10.1371/currents.dis.4250a225860babf3601a18e33e172d8b>.
- Panitz, H.-J., A. Dosio, M. Büchner, D. Lüthi, and K. Keuler, 2014: COSMO-CLM (CCLM) climate simulations over CORDEX-Africa domain: Analysis of the ERA-Interim driven simulations at 0.44 and 0.22 resolution. *Climate Dyn.*, **42**, 3015–3038, <https://doi.org/10.1007/s00382-013-1834-5>.
- Perkins, S., A. Pitman, N. Holbrook, and J. McAneney, 2007: Evaluation of the AR4 climate models' simulated daily maximum temperature, minimum temperature, and precipitation over Australia using probability density functions. *J. Climate*, **20**, 4356–4376, <https://doi.org/10.1175/JCLI4253.1>.
- Petković, V., and C. D. Kummerow, 2017: Understanding the sources of satellite passive microwave rainfall retrieval systematic errors over land. *J. Appl. Meteor. Climatol.*, **56**, 597–614, <https://doi.org/10.1175/JAMC-D-16-0174.1>.
- Prakash, S., A. K. Mitra, D. Pai, and A. AghaKouchak, 2016: From TRMM to GPM: How well can heavy rainfall be detected from space? *Adv. Water Resour.*, **88**, 1–7, <https://doi.org/10.1016/j.advwatres.2015.11.008>.
- Prein, A. F., A. Gobiet, M. Suklitsch, H. Truhetz, N. Awan, K. Keuler, and G. Georgievski, 2013: Added value of



- convection permitting seasonal simulations. *Climate Dyn.*, **41**, 2655–2677, <https://doi.org/10.1007/s00382-013-1744-6>.
- , and Coauthors, 2015: A review on regional convection-permitting climate modeling: Demonstrations, prospects, and challenges. *Rev. Geophys.*, **53**, 323–361, <https://doi.org/10.1002/2014RG000475>.
- Quagraine, K. A., F. Nkrumah, C. Klein, N. A. B. Klutse, and K. T. Quagraine, 2020: West African summer monsoon precipitation variability as represented by reanalysis datasets. *Climate*, **8**, 111, <https://doi.org/10.3390/cli8100111>.
- Roller, S., H. Wittmann, M. Kastowski, and M. Hinderer, 2012: Erosion of the Rwenzori Mountains, East African Rift, from in situ-produced cosmogenic <sup>10</sup>Be. *J. Geophys. Res. Earth Surf.*, **117**, F03003, <https://doi.org/10.1029/2011JF002117>.
- Rooney, G. G., N. P. M. Van Lipzig, and W. Thiery, 2018: Estimating the effect of rainfall on the surface temperature of a tropical lake. *Hydrol. Earth Syst. Sci.*, **22**, 6357–6369, <https://doi.org/10.5194/hess-22-6357-2018>.
- Sahlu, D., E. I. Nikolopoulos, S. A. Moges, E. N. Anagnostou, and D. Hailu, 2016: First evaluation of the Day-1 IMERG over the upper Blue Nile basin. *J. Hydrometeorol.*, **17**, 2875–2882, <https://doi.org/10.1175/JHM-D-15-0230.1>.
- Schneider, U., A. Becker, P. Finger, A. Meyer-Christoffer, M. Ziese, and B. Rudolf, 2014: GPCC's new land surface precipitation climatology based on quality-controlled in situ data and its role in quantifying the global water cycle. *Theor. Appl. Climatol.*, **115**, 15–40, <https://doi.org/10.1007/s00704-013-0860-x>.
- Sillmann, J., V. V. Kharin, X. Zhang, F. Zwiers, and D. Bronaugh, 2013: Climate extremes indices in the CMIP5 multimodel ensemble: Part 1. Model evaluation in the present climate. *J. Geophys. Res. Atmos.*, **118**, 1716–1733, <https://doi.org/10.1002/jgrd.50203>.
- Silva, V. B., V. E. Kousky, W. Shi, and R. W. Higgins, 2007: An improved gridded historical daily precipitation analysis for Brazil. *J. Hydrometeorol.*, **8**, 847–861, <https://doi.org/10.1175/JHM598.1>.
- Sungmin, O., and P.-E. Kirstetter, 2018: Evaluation of diurnal variation of GPM IMERG-derived summer precipitation over the contiguous US using MRMS data. *Quart. J. Roy. Meteor. Soc.*, **144** (Suppl. 1), 270–281, <https://doi.org/10.1002/qj.3218>.
- Tabari, H., and Coauthors, 2016: Local impact analysis of climate change on precipitation extremes: Are high-resolution climate models needed for realistic simulations? *Hydrol. Earth Syst. Sci.*, **20**, 3843–3857, <https://doi.org/10.5194/hess-20-3843-2016>.
- , N. M. Asr, and P. Willems, 2021: Developing a framework for attribution analysis of urban pluvial flooding to human-induced climate impacts. *J. Hydrol.*, **598**, 126352, <https://doi.org/10.1016/j.jhydrol.2021.126352>.
- Tan, J., W. A. Petersen, and A. Tokay, 2016: A novel approach to identify sources of errors in IMERG for GPM ground validation. *J. Hydrometeorol.*, **17**, 2477–2491, <https://doi.org/10.1175/JHM-D-16-0079.1>.
- , G. J. Huffman, D. T. Bolvin, and E. J. Nelkin, 2019a: Diurnal cycle of IMERG V06 precipitation. *Geophys. Res. Lett.*, **46**, 13 584–13 592, <https://doi.org/10.1029/2019GL085395>.
- , —, —, and —, 2019b: IMERG V06: Changes to the morphing algorithm. *J. Atmos. Oceanic Technol.*, **36**, 2471–2482, <https://doi.org/10.1175/JTECH-D-19-0114.1>.
- Tan, M. L., N. Samat, N. W. Chan, and R. Roy, 2018: Hydro-meteorological assessment of three GPM satellite precipitation products in the Kelantan River Basin, Malaysia. *Remote Sensing*, **10**, 1011, <https://doi.org/10.3390/rs10071011>.
- Tan, X., B. Yong, and L. Ren, 2018: Error features of the hourly GSMaP multi-satellite precipitation estimates over nine major basins of China. *Hydrol. Res.*, **49**, 761–779, <https://doi.org/10.2166/nh.2017.263>.
- , Z. Ma, K. He, X. Han, Q. Ji, and Y. He, 2020: Evaluations on gridded precipitation products spanning more than half a century over the Tibetan Plateau and its surroundings. *J. Hydrol.*, **582**, 124455, <https://doi.org/10.1016/j.jhydrol.2019.124455>.
- Thiery, W., A. Martynov, F. Darchambeau, J.-P. Descy, P.-D. Plisnier, L. Sushama, and N. P. M. Van Lipzig, 2014a: Understanding the performance of the FLake model over two African Great Lakes. *Geosci. Model Dev.*, **7**, 317–337, <https://doi.org/10.5194/gmd-7-317-2014>.
- , and Coauthors, 2014b: LakeMIP Kivu: Evaluating the representation of a large, deep tropical lake by a set of one-dimensional lake models. *Tellus*, **66A**, 21390, <https://doi.org/10.3402/tellusa.v66.21390>.
- , E. L. Davin, H.-J. Panitz, M. Demuzere, S. Lhermitte, and N. P. M. Van Lipzig, 2015: The impact of the African Great Lakes on the regional climate. *J. Climate*, **28**, 4061–4085, <https://doi.org/10.1175/JCLI-D-14-00565.1>.
- , L. Gudmundsson, K. Bedka, F. H. Semazzi, S. Lhermitte, P. Willems, N. P. M. Van Lipzig, and S. I. Seneviratne, 2017: Early warnings of hazardous thunderstorms over Lake Victoria. *Environ. Res. Lett.*, **12**, 074012, <https://doi.org/10.1088/1748-9326/aa7521>.
- Tiedtke, M., 1989: A comprehensive mass flux scheme for cumulus parameterization in large-scale models. *Mon. Wea. Rev.*, **117**, 1779–1800, [https://doi.org/10.1175/1520-0493\(1989\)117<1779:ACMFSF>2.0.CO;2](https://doi.org/10.1175/1520-0493(1989)117<1779:ACMFSF>2.0.CO;2).
- , 1993: Representation of clouds in large-scale models. *Mon. Wea. Rev.*, **121**, 3040–3061, [https://doi.org/10.1175/1520-0493\(1993\)121<3040:ROCILS>2.0.CO;2](https://doi.org/10.1175/1520-0493(1993)121<3040:ROCILS>2.0.CO;2).
- Tompkins, A. M., K. Gierens, and G. Rädcl, 2007: Ice supersaturation in the ECMWF integrated forecast system. *Quart. J. Roy. Meteor. Soc.*, **133**, 53–63, <https://doi.org/10.1002/qj.14>.
- Uganda Wildlife Authority, 2020: Rwenzori Mountains National Park. UWA, accessed 23 April 2022, <https://ugandawildlife.org/tours/rwenzori-mountains/>.
- Vanden Broucke, S., and N. P. M. Van Lipzig, 2017: Do convection-permitting models improve the representation of the impact of LUC? *Climate Dyn.*, **49**, 2749–2763, <https://doi.org/10.1007/s00382-016-3489-5>.
- , H. Wouters, M. Demuzere, and N. P. M. Van Lipzig, 2019: The influence of convection-permitting regional climate modeling on future projections of extreme precipitation: Dependency on topography and timescale. *Climate Dyn.*, **52**, 5303–5324, <https://doi.org/10.1007/s00382-018-4454-2>.
- Vanderkelen, I., N. P. M. Van Lipzig, and W. Thiery, 2018a: Modelling the water balance of Lake Victoria (East Africa)—Part 1: Observational analysis. *Hydrol. Earth Syst. Sci.*, **22**, 5509–5525, <https://doi.org/10.5194/hess-22-5509-2018>.
- , —, and —, 2018b: Modelling the water balance of Lake Victoria (East Africa)—Part 2: Future projections. *Hydrol. Earth Syst. Sci.*, **22**, 5527–5549, <https://doi.org/10.5194/hess-22-5527-2018>.
- Van de Walle, J., W. Thiery, O. Brousse, N. Souverijns, M. Demuzere, and N. P. M. Van Lipzig, 2020: A convection-permitting model for the Lake Victoria Basin: Evaluation and insight into the mesoscale versus synoptic atmospheric dynamics.

- Climate Dyn.*, **54**, 1779–1799, <https://doi.org/10.1007/s00382-019-05088-2>.
- Wu, Y., L. Guo, H. Zheng, B. Zhang, and M. Li, 2019: Hydroclimate assessment of gridded precipitation products for the Tibetan Plateau. *Sci. Total Environ.*, **660**, 1555–1564, <https://doi.org/10.1016/j.scitotenv.2019.01.119>.
- Xu, R., F. Tian, L. Yang, H. Hu, H. Lu, and A. Hou, 2017: Ground validation of GPM IMERG and TRMM 3B42V7 rainfall products over southern Tibetan Plateau based on a high-density rain gauge network. *J. Geophys. Res. Atmos.*, **122**, 910–924, <https://doi.org/10.1002/2016JD025418>.
- Yang, W., R. Seager, M. A. Cane, and B. Lyon, 2015: The rainfall annual cycle bias over East Africa in CMIP5 coupled climate models. *J. Climate*, **28**, 9789–9802, <https://doi.org/10.1175/JCLI-D-15-0323.1>.
- Yatagai, A., K. Minami, M. Masuda, and N. Sueto, 2019: Development of intensive aphrodite hourly precipitation data for assessment of the moisture transport that caused heavy precipitation events. *Sci. Online Lett. Atmos.*, **15A**, 43–48, <https://doi.org/10.2151/sola.15A-008>.
- Zhang, L., P. Wu, T. Zhou, M. J. Roberts, and R. Schiemann, 2016: Added value of high resolution models in simulating global precipitation characteristics. *Atmos. Sci. Lett.*, **17**, 646–657, <https://doi.org/10.1002/asl.715>.
- Zhang, X., L. Alexander, G. C. Hegerl, P. Jones, A. K. Tank, T. C. Peterson, B. Trewin, and F. W. Zwiers, 2011: Indices for monitoring changes in extremes based on daily temperature and precipitation data. *Wiley Interdiscip. Rev.: Climate Change*, **2**, 851–870, <https://doi.org/10.1002/wcc.147>.
- Zhang, Y., V. Dulière, P. W. Mote, and E. P. Salathé Jr., 2009: Evaluation of WRF and HadRM mesoscale climate simulations over the U.S. Pacific Northwest. *J. Climate*, **22**, 5511–5526, <https://doi.org/10.1175/2009JCLI2875.1>.